Physics – Uspekhi **52** (1) 29 – 54 (2009)

REVIEWS OF TOPICAL PROBLEMS PACS numbers: **61.46.–w**, 62.20.Qp, **62.25.–g**

Structures and properties of hard and superhard nanocomposite coatings

A D Pogrebnjak, A P Shpak, N A Azarenkov, V M Beresnev

DOI: 10.3367/UFNe.0179.200901b.0035

Contents

Abstract. Various approaches to creating multicomponent nanocomposite coatings of high and superhigh hardness (from ≃ 30 to 100 – 120 GPa) are reviewed with particular emphasis placed on mechanisms underlying the increase in hardness in thin (⩽ 10 μm) coatings. The deposition technologies considered include magnetron sputtering, ion beam-assisted and vacuum arc depositions. A classification of hard and superhard coatings with high thermal stability is given. Possible applications of such nanostructured coatings are discussed and prospects for the field are outlined.

A D Pogrebnjak, A P Shpak G V Kurdyumov Institute for Metal Physics, National Academy of Sciences of Ukraine,
pl. Ac. Vernadskogo 36, 252680 Kyiv, Ukraine
Tel. +38 (054) 278 39 86, +38 (068) 160 69 89,
E-mail: apogrebnjak@simp.sumy.ua, alexp@i.ua
N A Azarenkov, V M Beresnev V N Karazin Kharkiv National University,
pl. Svobody 4, 61077 Kharkiv, Ukraine
Tel. +38 (057) 720 32 52, +38 (050) 641 60 35, +38 (057) 706 33 35
E-mail: scpt@bi.com.ua; azarenkov@univer.kharkov.ua

Received 14 February 2008, revised 3 July 2008
Uspekhi Fizicheskikh Nauk **179** (1) 35 – 64 (2008)
DOI: 10.3367/UFNr.0179.200901b.0035
Translated by Yu V Morozov; edited by A Radzig

1. Introduction

Creation of new materials, including multicomponent nanocomposite coatings with a characteristic grain size below 100 nm, is a priority area of modern science and technology. Nanotechnologies are expected to become the principal driving force in scientific and technical developments by the mid-21st century. Nanothechnology is a field focusing on the control of matter on the atomic, molecular, and supramolecular scales (in a range of sizes from 1 to 50 nm) for the creation, processing, and application of materials, devices, and systems having novel properties and functional capabilities due to the small size of their structural elements [1 – 5]. From the physical standpoint, passage to the nanostate is associated with the appearance of dimensional effects understood as a series of phenomena brought about by changes in the properties of matter arising from the coincidence between the block size of a microstructure and a certain critical length that characterizes a given phenomenon (mean free paths of electrons and photons, domain wall thickness, critical radius of the dislocation loop, etc.).

Dimensional effects show themselves when the average size of crystalline grains is below 50 nm; they are especially well apparent as the grain size approaches less than 10 nm. Table 1 presents selected size-dependent properties of materi-

Table 1. Size-dependent physical properties of materials.

Properties	Response of material to a decrease in the grain size
Thermal	Lowered phase transition temperature, including melting temperature
Kinetic	Abnormally high diffusion coefficients; reduced heat conductivity
Electrical	Enhanced electrical conduction in ceramics; enhanced metallic resistance
Magnetic	Increased coercive force
Mechanical	Reduced moduli of elasticity; elevated yield point, hardness, fracture toughness, and wear resistance; superplasticity behavior at high temperatures

als [6 – 10]. In this context, nanomaterials may be classified by the size and geometric shape of their structural elements. The main types of nanomaterials in terms of grain size are cluster and fiber materials, films and coatings, multilayer (multicomponent) structures, and bulk nanocrystalline materials whose grains have nanometer dimensions in all three directions [1 – 19].

The present review being focused on hardened nanocomposite coatings, it should first of all be emphasized that the unique nature of these nanostructured and nanocomposite coatings is due to the strength and large volume fraction of interphase boundaries in the absence of dislocations inside crystallites, the possibility of changing the volume fraction ratio of crystalline and amorphous phases, and the mutual solubility of metal and nonmetal components [7 – 12]. For example, a large interface area (at a volume fraction amounting to $\lesssim 50\%$) in nanocomposite coatings and films allows their properties to be substantially altered both by modification of morphology and electronic structure and by doping with different elements [1 – 4, 7, 19]. The strength of interphase boundaries promotes strain resistance of nanostructured (nanocomposite) coatings. The absence of dislocations inside crystallites increases coating elasticity. All these properties allow for obtaining on the base of such coatings nanocomposite materials with improved physico-chemical and physico-mechanical properties such as high hardness ($H > 40$ GPa), elastic recovery ($H > 70\%$), strength, and heat and corrosion resistance [7, 12, 13 – 17]. A very important feature of superhard nanocomposite coatings is that equally hard materials may differ in elasticity modulus (E), resistance to elastic breakdown (H/E), and plastic resistance (H^3/E^2) (see, for instance, Refs [5 – 12, 18]).

Veprek and coworkers [19] framed a concept for the production of superhard nanocrystalline nanocomposite coatings whereby they must be composed of dislocation-free nanocrystallites (solid phases) of size 3 – 10 nm separated by a 1 – 3 nm-sized amorphous phase interlayer. The ideal model of a superhard nanocomposite coating is illustrated in Fig. 1a [7]; Fig. 1b presents a schematic of one of the nanocomposites in the Ti – Si – N system (see references in report [9]).

The nanocomposite consists of an amorphous silicon nitride (Si_3N_4) matrix [19] with inclusions of TiN nanocrystallites and $TiSi_2$ precipitations, either nanocrystalline or amorphous, at triple junctions between titanium nitride grains [4, 7, 18, 19]. It should be noted that traditional dispersion-strengthened alloys having nano-sized inclusions of particles with a volume faction of only 5 – 20% in their structure are not regarded as nanomaterials [15 – 18].

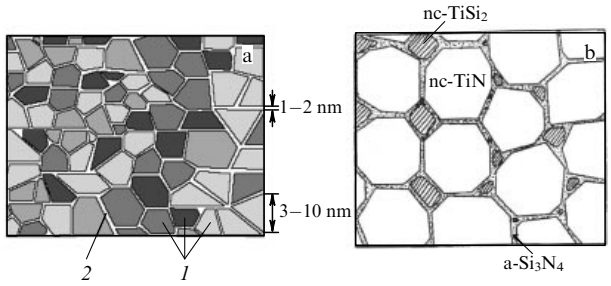

Figure 1. (a) Idealized nanostructured coating suggested by Veprek et al. [7], and (b) schematic of the nc-TiN/a-Si_3N_4/nc-$TiSi_2$ structure [127].

With this in mind, the aim of the present review is to demonstrate various approaches to the formation of hard and superhard coatings and their analysis from the perspective of the general principles of production, investigation into physico-chemical and physico-mechanical properties, and the prospects of practical application.

2. Hardness-enhanced nanocomposite coatings

Nanocomposite coatings exemplify materials of a new generation, composed of at least two phases with a nanocrystalline and/or amorphous structure. Because of the very small size ($\leqslant 10$ nm) of their grains and more important role of boundary zones surrounding single grains, nanocomposite materials behave unlike traditional materials with a grain size over 100 nm and display quite different properties. The novel unique physical and functional properties of nanocomposites constitute a driving force for the rapid development of nanocomposite materials [20 – 30]. Films with the hardness $H \leqslant 40$ GPa and $H > 40$ GPa are currently described as hard and superhard, respectively.

As is known, there are two groups of hard and superhard nanocomposites, viz. nc-*Me*H/hard phase and nc-*Me*H/soft phase. Moreover, bi-crystalline phases and/or phases with two crystallographic orientations of the grains in the same material are distinguished in nanocrystalline and/or amorphous phases. The concept of nanocomposites possessing enhanced hardness was formulated using these insights. The microstructure of one- and two-phase films is essentially different. Let us consider the concept of Musil and coworkers [28 – 38] that takes into account the influence of the geometry of nanostructural features, such as grain size and crystallite shape.

2.1 Enhanced hardness

2.1.1 Mechanism of hardness enhancement. The main factors responsible for enhanced hardness H of nanostructures are plastic deformation with the leading role of dislocations, cohesive forces acting between atoms, and compression macrostresses σ generated in the course of film formation. Macrostresses are undesirable and can be avoided by close control over the film deposition process. Hardness depends on the type of the process dominating in a given grain size range (Fig. 2). There is a critical characteristic size of nanocrystallites, $d_c \sim 10$ nm, at which maximum hardness H_{max} can be achieved. The existence of such a characteristic nanocrystallite size ensuring maximum hardness of nanocomposite coatings or films is due to the continuous transition, at values around d_c, from microscopic processes

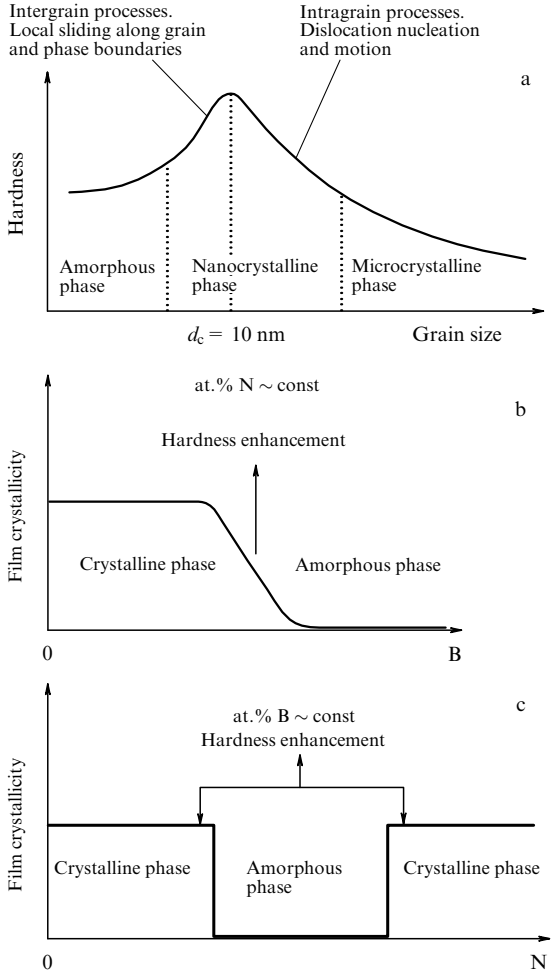

Figure 2. (a) Schematic representation of material hardness as a function of grain size d [119, 195, 196]. (b, c) Transition regions in the $A_{1-x}B_xN$ compound: regions of transition from crystalline to amorphous phase (b) and between two crystalline phases or two main crystallographic orientations of the grains (c) [119, 195, 196, 35–38].

of dislocation nucleation and motion (for $d > d_c$) described by the known Hall–Petch law $H \sim d^{-1/2}$ for conventional polycrystalline materials to intercrystallite processes of local sliding along grain and phase boundaries (for $d < d_c$).

It is generally accepted that nanocrystallites smaller than 10 nm do not have dislocation multiplication sources. It is also believed that the characteristic size of nanocrystallites as applied to nanocrystalline metallic materials lies in a range from 2 to 34 nm (see papers cited in Refs [7, 13]).

2.1.2 Formation of nanostructured films. Nanocrystalline films produce low-intensity diffuse X-ray reflectance bands. Such films are formed in the so-called transition regions where their structure is substantially altered. There are three groups of transition states, viz. (1) transition from a crystalline to an amorphous phase, (2) transition between two phases of different materials, and (3) transition between two main orientations of the grains in one and the same material (Fig. 2b, c).

2.1.3 Structure of nanocomposites. Hardness-enhanced nanocomposites may have different structures (Fig. 3). Group 1 nanocomposites (according to the classification in Section 2.1.2) are composed of columnar (Fig. 3a) or nanocrystalline (nc) grains surrounded by thin multilayer phases equivalent to the bulk material (Fig. 3b; the amount of B in $Al_{1-x}B_xN$ compared with that in Fig. 3a). Columnar structures are normal to the substrate/film interface. Nanocomposites of groups 2 and 3 that formed at the edges of well-apparent transitions also possess a nanocolumnar structure (Fig. 3b). In contrast, nanocomposites of groups 2 and 3 that formed inside such a transition comprise a mixture of micrograins and have a compact globular structure (Fig. 3c).

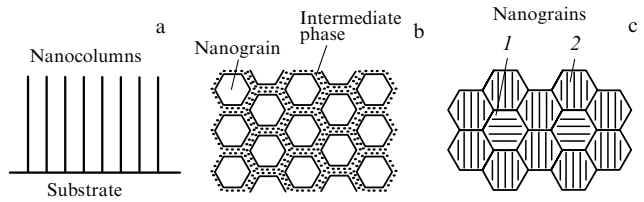

Figure 3. Structural organization of the nanocomposites with enhanced hardness: (a) columnar, (b) nanograins embedded in a phase equivalent to the bulk material, and (c) a mixture of nanograins.

Nanocomposites exhibiting enhanced hardness fall into three groups:

(1) Nanocomposites composed of grains assembled in columnar structures; the amount of the secondary (second) phase of the bulk material is insufficient to totally cover the surface of all grains (Fig. 3a).

(2) Nanocomposites with a compact globular structure comprising nanograins completely enclosed in the bulk material (Fig. 3b).

(3) Nanocomposites with a compact globular structure comprising nanograins of different materials or nanograins with different crystallographic orientations and/or lattice structures formed from one and the same material (Fig. 3c).

This experimentally verified classification clearly indicates that hardness enhancement is directly related to the size and the shape of the 'building blocks' of which the nanocomposites are composed. The geometry of these grains is of paramount importance.

2.2 Mechanical properties of nanocomposite coatings

The main characteristics describing the mechanical properties of nanocomposite coatings are hardness H, effective Young modulus $E^* = E/(1-\nu^2)$, and elastic aftereffect (recovery) W_e; here, E is the Young modulus, and ν is the Poisson ratio. These quantities can be computed from the loading/unloading curve measured by a microdurometer. Experimental H and E^* values are used to calculate the H^3/E^{*2} ratio. H and E^* are proportional to the plastic resistance of the material [31]. Plastic deformation is unessential in materials with high hardness and a low effective Young modulus. In the general case, a low Young modulus enables a given load to spread over a wide area beneath the indenter.

Dependences $H=f(E^*)$, $H^3/E^{*2}=f(H)$, and $W_e=f(H)$ are the main relationships describing the mechanical properties of thin films [24, 27, 32]. They are shown for selected oxides, carbides, and nitrides in Fig. 4. It follows from Fig. 4a that the dependence $H=f(E^*)$ can be approximated by a straight line:

$$H\,(\mathrm{GPa}) = 0.15E^* - 12\,(\mathrm{GPa})\,. \qquad (1)$$

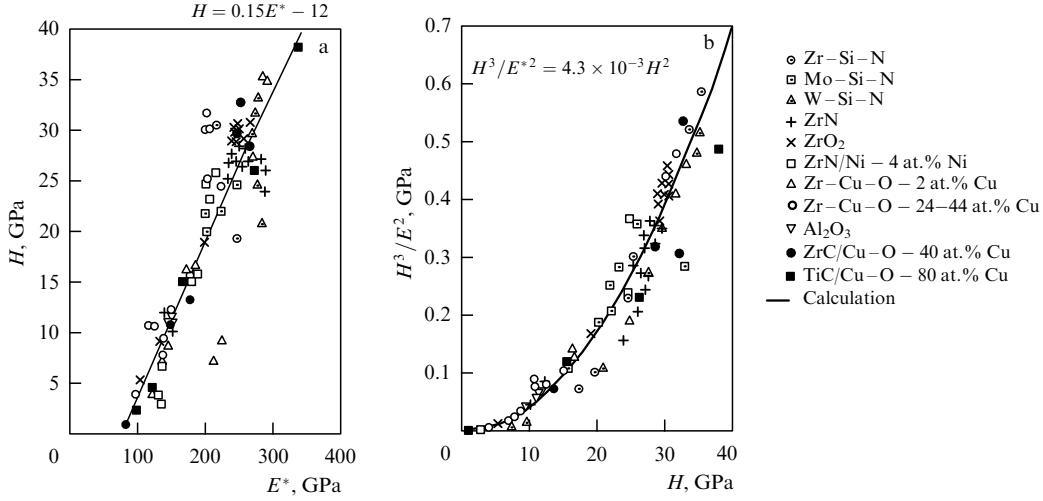

Figure 4. Relationship between H and E^* (a) and between H^3/E^* and H (b) for selected oxides, carbides, and nitrides obtained by magnetron sputtering under different conditions [56].

Dependence $H^3/E^{*2} = f(H)$ in Fig. 4b is approximated by the following empirical formula:

$$\frac{H^3}{E^{*2}} = 4.3 \times 10^{-3} H^2 . \quad (2)$$

The experimental points fairly well fit the lines defined by formulas (1) and (2). This discovery may have fundamental significance for the prediction of mechanical behavior of coatings. First, all materials shown in Fig. 4 are characterized by strict correspondence between H and E^*, i.e., H grows almost linearly with increasing E^* (Fig. 4a). The scatter in the experimental data around the straight line may have a different origin and needs an in-depth study that is beyond the scope of this review. Second, film hardness H_f is not exactly equal to $0.1E^*$, while $H_f \leqslant 0.1E^*$ for $E^* \leqslant 240$ GPa, and $H_f \geqslant 0.1E^*$ for $E^* \geqslant 240$ GPa. This precludes control of the film's mechanical behavior, for example, its plastic resistance. This fact shows that the basic relationship between H and E^* given by Eqns (1) and (2) can be used to elucidate the relationship between film cracking and viscosity. This issue is addressed in greater detail in Ref. [33].

In conclusion, the mechanical properties of nanocomposite coatings strongly depend on the elements forming separate phases, the relative amount of different phases, their chemical interactions, and their microstructure. See papers [24, 27, 32] for details.

2.3 Behavior of hard nanocomposite coatings at high temperatures

2.3.1 Thermal stability of the properties. As noted in Section 2.1.3, the unique properties of nanocomposite films directly arise from their nanostructure. However, the nanostructure constitutes a metastable phase: if the temperature at which a film forms exceeds a certain threshold value T_c its material undergoes crystallization, leading to the destruction of the nanostructure and the appearance of new crystalline phases that account for the loss of unique properties by nanocomposite films for $T > T_c$. In other words, temperature T_c at which the nanostructure turns to the crystalline phase determines the thermal stability of a given nanocomposite. However, these materials not infrequently have to be employed at temperatures above 1000 °C, hence the necessity to develop new ones with maximum thermal stability in excess of 1000 °C.

2.3.2 Resistance to high-temperature oxidation. Oxidation resistance is a most attractive property of hard nanocomposite coatings. Oxidation resistance of hard films strongly depends on their elemental composition. Figure 5 illustrates the increase in the film weight Δm as a function of annealing temperature T. The temperature at which Δm sharply increases is described as maximum temperature T_{max} at which film oxidation can be avoided. The higher T_{max}, the greater the oxidation resistance. All the films represented in Fig. 5 and characterized by a sharp growth in Δm with increasing temperature are crystalline or nanocrystalline. All of them possess oxidation resistance T_{max} below 1000 °C. This is not surprising, since they are composed of grains that are constantly in contact with the air through grain boundaries at the film/substrate interface. This phenomenon sharply decreases oxidation resistance in the bulk of the film and is thereby responsible for the impaired efficiency of the barrier formed by the upper layer of an oxide film. For all that, an improvement is feasible by the utilization of the intergranular vitreous phase.

Thus far, only one efficacious method for increasing oxidation resistance in hard coatings is known, namely, interruption of the continuous path along grain boundaries from the coating surface to the underlying substrate across the bulk. It is possible to realize in solid amorphous films such as those formed by a new family of composites a-Si_3N_4/MeN_x with a high content (> 50 vol.%) of the amorphous phase a-Si_3N_4 [35 – 38]. This possibility is illustrated by Fig. 5b, c showing a polished section of nanocomposite Ta – Si – N and Mo – Si – N films. Change in mass Δm remains practically unaltered after annealing the Ta – Si – N film at temperatures up to 1300 °C (Fig. 5a).

2.3.3 Amorphous nanocomposites resistant to high-temperature oxidation. Nanocomposites containing > 50 vol. % of silicon nitride are amorphous (Fig. 5b, c). It can be seen that the bulk of the Ta – Si – N film possesses an amorphous structure and only the surface of the film underwent oxidation; the oxide

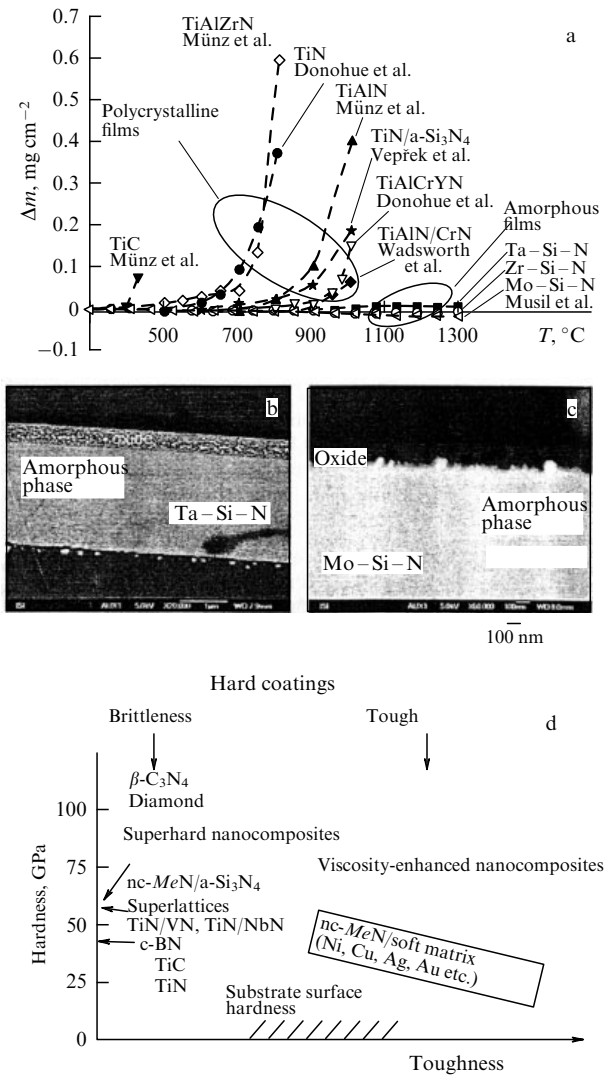

Figure 5. (a) Oxidation resistance of selected hard coatings, characterized by the dependence of Δm on annealing temperature T [33, 34, 37, 38]. Polished section of Ta – Si – N (b) [35] and Mo – Si – N (c) [36] films on an Si (100) substrate after high-temperature annealing in flowing air at $T = 1300\,^{\circ}$C. (d) Classification of nanocomposites by hardness and viscosity.

surface layer of Ta_2O_5 is about 400 nm thick. This film exhibits the highest oxidation resistance (Fig. 5a); its hardness H varies from 20 to 40 GPa. Such characteristics of Ta – Si – N films account for the wide range of their applications, e.g., as protective coatings for cutting tools.

However, a high content of silicon nitride phase alone is not sufficient to ensure resistance to high-temperature oxidation. Certain elements, like Mo, W and some others, tend to form volatile oxides released from a nanocomposite upon oxidation. This results not only in the formation of a porous structure of the oxide layer surface (Fig. 5b, c) but also in impaired oxidation resistance. The pores appear because newly formed volatile oxides MoO_x diffuse to the outside from the surface layer at $T = 800-1000\,^{\circ}$C. But the main cause of impaired oxidation resistance is disintegration of the metal nitride (MeN_x) phase in the nanocomposite; hence the importance of choosing films with proper elemental composition.

Oxidation resistance at maximum annealing temperatures can be achieved by ensuring high thermal stability of both phases in a given nanocomposite, i.e., of amorphous silicon nitride against crystallization and of metal nitride against degradation ($MeN_x \rightarrow Me + N_2$). In this context, such nanocomposites as Zr – Si – N [35], Ta – Si – N [34], and Ti – Si – N with a high (> 50 vol.%) silicon nitride phase content, as well as silicon oxide- and oxynitride-based nanocomposites, appear especially promising.

2.4 Viscosity of thin nanocomposite coatings

Hardness is one of the most important mechanical properties, but it is by far insufficient to choose one material or another for a concrete application. In many cases, viscosity is even more important. Hence, there is a necessity to manufacture films combining hardness with viscosity (Fig. 5d).

Viscosity determines the ability of a material to absorb energy during deformation to complete disintegration. It can be enhanced by retarding or reducing crack initiation and propagation. There are several ways to reach this goal: (1) to impart plasticity to phase toughness by introducing some plastic phases (metals) into ceramic matrices; (2) to use impact plasticity of nanophases based on crack refraction and branching or sliding along grain boundaries; (3) to use impact plasticity of multilayer structures based on the alternation of numerous brittle and viscous thin layers; (4) to create conditions for the development of fiber or nanotubular toughness based on cross-linking bonds or crack defocusing; (5) to use toughness at which part of the absorbed energy is utilized to support phase transformations, and (6) to use toughness at compressive stresses and thereby prevent the onset of initiating cracks by their healing.

The main problem to date is to determine toughness of thin films. It has recently been shown that toughness of thin films can be estimated without their destruction by microindentation. It turned out that the H^3/E^{*2} ratio is important. See Refs [29, 33] for details.

3. Physical and mechanical properties of sputtered Ta – Si – N films with high (> 40 at.%) Si content

Ta – Si – N films are used as barriers to diffusion between Cu and Si in integrated circuit technology by virtue of their amorphous structure and high thermal stability [39, 40]. Good mechanical properties and high oxidation resistance make Ta – Si – N films suitable as protective coatings. Silicon stabilizes the amorphous structure of the film and improves its mechanical properties, such as hardness and adhesive force [41]. The compound Si_3N_4 forms in deposited films and combines with a part of (Ta, Si)N [42]. Ta – Si – N films with low Si content (7 at.%) are thermally stable up to 900 °C, when their crystallization begins. Recrystallization results in the formation of intermetallic Ta_2N, Ta_5Si, and Ta_5Si_3 phases [43].

3.1 Magnetron sputtering plating rate

The dependence of film deposition rate a_d on nitrogen partial pressure p_{N_2} at different bias voltages U_s on the substrate, ion currents i_s on the substrate, and discharge currents I_d is illustrated by Fig. 6a.

It can be seen that a_d for all films is independent of pressure for $p_{N_2} < 0.25$ Pa but decreases for $p_{N_2} > 0.25$ Pa as a result of target etching. The value of a_d grows with increasing I_d. The deposition rate for films obtained at discharge power $P_d = 800$ W, $i_s = 1$ mA cm^{-2}, and $U_s = -100$ V is higher

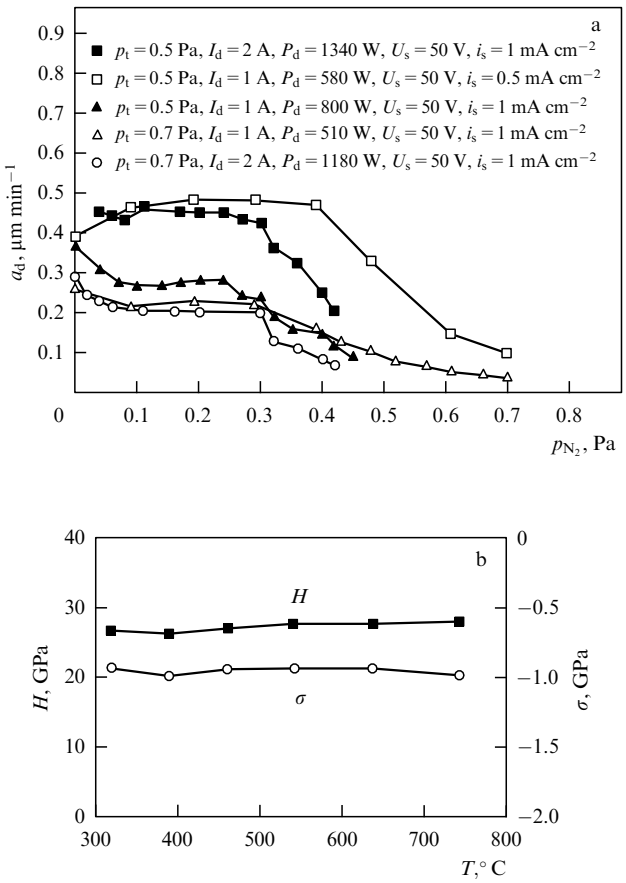

Figure 6. Dependence of deposition rate a_d on p_{N_2} for Ta – Si – N films deposited at $T_s = 500\,°C$ and different combinations of I_d, U_s, i_s, and p_t. (a) Microhardness H and macrostress σ of 3-μm-thick films deposited at $I_d = 1$ A, $U_s = -50$ V, $i_s = 1$ mA cm^{-2}, $p_{N_2} = 0.2$ Pa, and $p_t = 0.5$ Pa as functions of substrate temperature T_s. (b) Hardness was measured when a load of 50 mN was applied to a diamond indenter.

than for films deposited at $P_d = 560$ W, $i_s = 0.5$ mA cm^{-2}, and $U_s = -50$ V due to greater plasma density in the former.

3.2 Mechanical properties and macrostresses

The dependences of hardness H of Ta – Si – N films and macrostress σ generated in films growing at substrate temperature T_s are depicted in Fig. 6b. All the films had equal thickness $h \sim 3$ μm. It follows from Fig. 6b that hardness is practically independent of substrate temperature T_s in a wide range from 300 to 750 °C and is rather high, $H \sim 27$ GPa. The effective Young modulus and elastic recovery are also constant: $E^* \sim 250$ GPa, and $W_e \sim 65\%$, respectively. Compressive macrostress σ is low (on the order of -1 GPa) and also independent of T_s, suggesting the specific (amorphous) structure of Ta – Si – N films with a high Si content confirmed by X-ray diffraction data. It is supposed that the amorphous structure of these films is responsible for their high thermal stability.

3.3 Oxidation resistance

High-temperature oxidation resistance was studied using 4-μm-thick Ta – Si – N films deposited onto a substrate at $I_d = 1$ A, $U_s = 50$ V, $i_s = 1$ mA cm^{-2}, $T_s = 500\,°C$, $p_{N_2} = 0.43$ Pa, and $p_t = 0.7$ Pa (p_t is the overall pressure) (see Fig. 6a). The results suggest high oxidation resistance of the films studied. Weight gain at annealing temperature $T \sim 700\,°C$ was negligibly small. The oxidation rate began to increase when temperature exceeded 850 °C and reached roughly 0.125 μg cm^{-2} °C^{-1}. Slight oxidation of the Ta – Si – N films stopped at $T \sim 1100\,°C$ and remained constant for $T > 1100\,°C$ up to 1350 °C (the maximum temperature used in experiment [30]).

There are two explanations for such an arrest of the weight gain: (1) a stable passive oxide layer forms at the Ta – Si – N film surface or (2) the bulk of the film undergoes oxidation. The relative change in the weight being only 1.6%, the former explanation appears more plausible. This conjecture is confirmed by the formation of a thin smooth oxide interference layer at the Ta – Si – N film surface. Interference is responsible for the change of the surface color from blue to green with a rise in the annealing temperature from 850 to 1100 °C. Further elevation of the temperature from 1100 to 1350 °C produces no change in the color. The change of the film surface color with increasing T clearly indicates that oxidation results in the formation of a thin optically transparent oxide layer at the surface of the Ta – Si – N film, the thickness of which (~ 100 nm) is very small compared with the total film thickness (~ 4 μm). This layer stops growing when temperature exceeds 1100 °C. This barrier oxide layer prevents penetration of oxygen into the Ta – Si – N film and accounts for its very small weight gain ($\sim 1.6\%$) saturated for $T > 1100 - 1350\,°C$ (maximum temperature reached in the experiment). The hardness of the freshly sputtered Ta – Si – N film and its hardness after oxidation, measured under a load of 50 mN, were 26 and 16 GPa, respectively.

For comparison, Fig. 5a demonstrates the dependences of Δm on annealing temperature T, measured in the last 20 years by different authors [44 – 47]. Evidently, Ta – Si – N films exhibit the highest oxidation resistance, and increasing the degree of oxidation is virtually absent up to 1350 °C.

Ta – Si – N films with a high (> 40 at.%) Si content are amorphous and thermally stable up to $T_s = 750\,°$ (maximum substrate temperature used in experiments [30, 33]). These films are harder than bulk Si_3N_4 ($H_{Si_3N_4} = 17.2$ GPa) [48] and almost as hard as TaN and Ta_2N ($H_{TaN} \sim 32.4$ GPa, $H_{Ta_2N} = 30$ GPa) [49]. The electrical resistance of Ta – Si – N films increases with increasing p_{N_2}, but films obtained at $p_{N_2}/p_t \sim 1$ still retain the property of electrical conduction. Ta – Si – N films are characterized by high resistance to oxidation, and their weight does not grow significantly up to 1350 °C.

4. Relationship between elastically stressed state and the defective structure of nc-TiN – Cu and nc-AlN – Cu type hard coatings

This section presents results of the studies conducted by A D Korotaev and coworkers [50 – 52] using transmission electron microscopy (TEM) of the fine defect substructure and elastically stressed state of TiN, nc-TiN – Cu, and nc-AlN – Cu coatings obtained under identical conditions. The microstructure of the thin coating layer adjacent to the substrate in different parts of the surface is essentially nonuniform. It follows from annular electron diffraction patterns (Fig. 7b) and dark-field microphotographs (Fig. 7a) that its most characteristic feature is the nanocrystalline state with grains of size $d < 25$ nm and near-equiaxial shape. At the same time, certain parts exhibit a different type of structure as seen in quasiannular electron diffraction pat-

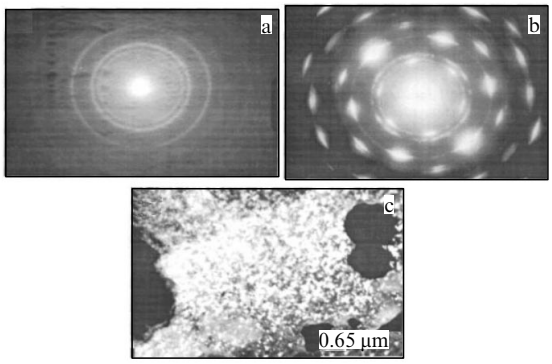

Figure 7. Dark-field images and electron diffraction patterns for TiN coatings (a) and TiN – Cu nanocomposites (b, c).

terns with bright (111) and (200) type structural maxima, giving the idea of prevailing crystal orientation. This structural feature is especially expressed in a TiN – Cu nanocomposite (Fig. 7c) with the constant size of crystallites.

Analysis of electron diffraction micropatterns with the substrate material preserved in the foil gives evidence of epitaxial nucleation of the coating on the substrates made from stainless steel and VT-20 alloy. A dark-field analysis showed that in this case TiN grains shaped as thin (dozens of nanometers) plates a fraction of micrometer in length lie almost parallel to the substrate surface.

An increase in the coating thickness results in a substantial change in the microstructure. A characteristic feature of electron microscopic contrast seen at a distance of 2 – 3 μm from the substrate matching surface is numerous extinction contours (Fig. 8a) that are in constant motion as the foil is tilted in the microscope column. In this case, no granular structure of the coating can be detected, although it is usually apparent from variations in diffraction contrast related to a change in crystal lattice orientation at grain boundaries. The curvature of crystallographic planes normal to the electron beam, $\chi_{ij} = 30$ deg μm^{-1}, was found from the shifts of extinction contours of reflections orthogonal to the projection of the tilt axis and from the change in the goniometer's tilt angle. Components of the curvature ($\chi_{ij} = 25 - 30$ deg μm^{-1}) of lattice planes parallel to the electron beam were also found by the method described in Ref. [79]. These findings suggest a high density of crystal structure defects and high local internal stresses in the coatings studied. Estimation of the excess density of dislocations having one and the same sign from the available χ_{ij} values (see paper [50] and references [17, 18] cited therein) gives $\rho = 10^{11}$ cm^{-2}.

High internal stresses are also evidenced by the microdiffraction picture (electron diffraction patterns display wide quasiannular reflections as shown in Fig. 8b). Moreover, splitting of (200) lines can be seen, indicative of a change in the lattice parameter: $\Delta a/a = 0.02$ (Fig. 8c). Local internal stresses $\sigma \sim E/50$ (E is the Young modulus) found from $\Delta a/a$ values prove to be of the same order of magnitude as those derived from χ_{ij} values.

Electron microscopic studies with the use of dark-field images gave evidence of a complex (two-level) coating structure. It turned out that TiN grains of submicron size ($d = 0.1 - 0.3$ μm) undergo fragmentation into 10 – 15-nm areas with the disorientation angle between them equal to $\theta < 5°$. In this case, regular fragment disorientation is found

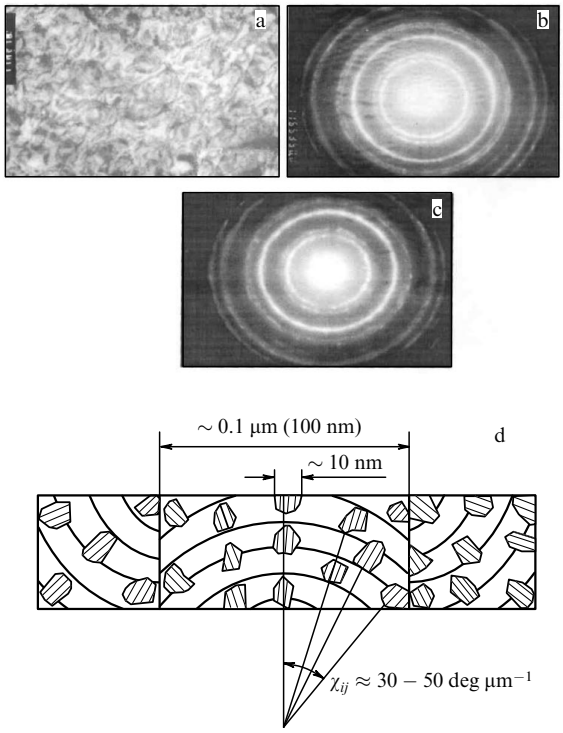

Figure 8. (a – c) Bright-field image of the structure and electron diffraction patterns from sections of a TiN – Cu nanocomposite coating with different internal stress levels at a distance of 2 – 3 μm from the substrate matching surface. (d) Schematic depiction of a submicrocrystal bend and fragmentation of the TiN – Cu nanocomposite coating.

to be analogous to that observed in polygonization of bent crystals. A bend and fragmentation of submicrocrystals are schematically shown in Fig. 8d.

A characteristic feature of the coatings under discussion is their well-apparent texture. The (111) texture is, as a rule, recognized from the line intensity ratio on electron diffraction patterns, although the (112) texture can also be seen in certain regions. X-radiography clearly reveals only a (111) texture. In particular, no (200) reflections were recorded in an nc-TiN – Cu compound with maximally intense (111) reflections.

The microstructure of AlN – Cu nanocomposite coatings is essentially different from that of the nc-TiN – Cu system considered above. To begin with, the substrate/coating matching surface exhibits a homogeneous nanocrystalline AlN phase with crystallite size $d < 20$ nm (Fig. 9b). The structure remains unaltered with the distance from the substrate matching surface. The width of rings in annular electron diffraction patterns does not change (Fig. 9c). Because the size of AlN crystallites measured from dark-field images of the microstructure does not change either, these data indicate that local internal stresses (microdistortions of the crystal lattice) do not substantially increase with increasing coating thickness. In this case, reflexes of a droplet fraction representing Al or $CuAl_2$ particles are better seen on annular electron diffraction patterns than near the substrate matching surface (Fig. 9c).

The size R and the volume concentration of particles in the droplet fraction characteristic of the above coatings were determined by scanning electron microscopy as equaling $\sim 0.1 - 0.2$ μm and 2 – 3%, respectively.

These experimental data suggest a significant difference in the structural evolution of growing nc-TiN – Cu

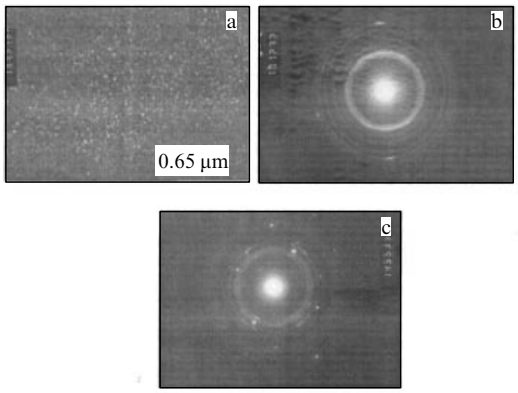

Figure 9. Dark-field image (a) and electron diffraction patterns of an AlN-Cu nanocomposite coating near the matching area with the substrate (b) and at a distance of 2 – 3 μm from the substrate (c).

and nc-AlN – Cu coatings. In aluminium nitride-based nanocomposites, multiple nucleation of randomly oriented AlN crystals and their growth to the size $d < 20-25$ nm occur both at the substrate matching surface and at the surface of the coating being formed. According to the authors of Refs [50 – 52], the immutable growth mechanism of coatings and their unaltered structure are responsible for the low level of local internal stresses. This opinion is confirmed by the invariable microstructure in dark- and bright-field images (compared with that at the substrate matching surface) and the width of rings of microdiffraction reflections (Fig. 9c). The texture in nc-TiN – Cu nanocomposites and single-phase TiN coatings is formed by the mechanism of columnar growth of TiN crystallites [52, 53, 55 – 57]. This process is associated with the formation of high local internal stresses responsible for the large horizontal and azimuthal curvature of lattice torsion, $\chi_{ij} = 30$ deg μm^{-1}, apparent from the presence of numerous thin extinction contours (Fig. 8a). Accordingly, a microstructural study by electron microscopy demonstrated the location of different grain portions in reflecting positions (Fig. 8a). Tilting the foil in the electron microscope column revealed continuous displacement of extinction contours and the corresponding portions of titanium nitride grains observed in the dark field. Sample tilting did not cause contours to shift at the grain boundaries, but thereafter they underwent a discrete change in position. These events can be used to determine the size ($d = 0.1-0.3$ μm) and the contours of individual grains.

As noted above, the dark-field microstructural study demonstrated grain fragmentation into 10 – 20-nm areas with the disorientation angle between fragments equal to $\theta < 5°$. Regular variation of fragment orientation gives reason to suggest that fragmentation is in fact the process of relaxation of the large ($\chi_{ij} = 30-50$ deg μm^{-1}) continuous lattice curvature by means of bent grain polygonization (Fig. 8c).

Thus, interactions during coating growth and changes in lattice orientation of columnar crystals give rise to a very large curvature and torsion of the lattice, $\chi_{ij} \leqslant 50$ deg μm^{-1}, and local internal stresses, $\sigma \sim G/30$ (G is the shear modulus), that partly relax upon formation of small-angle boundaries. Nevertheless, relaxation of internal stresses is incomplete. The authors of Refs [51, 52] observed spontaneous foil disintegration into micron-sized fragments as the coatings experienced ion thinning-down in the course of manufacturing thin foils. X-radiography studies revealed a 2% difference between lattice parameters in the directions normal and parallel to the coating surface. As shown above (see Fig. 8b), the width of diffraction lines greatly increased compared with those produced by coating layers adjacent to the substrate ($\Delta h \leqslant 15$ nm). Interestingly, the mean grain size ($d = 15$ nm) estimated by the Scherrer method from X-ray diffraction line width turned out to be of the same order of magnitude as that in a similar nc-TiN – Cu film [54, 58] despite considerable dispersion of appropriate values ($d = 12-18$ nm) for individual samples. Evidently, the grain size determined experimentally by X-ray test is consistent with the size of grain fragments reported in Ref. [50]. It appears that an increase in the lateral size during competitive columnar growth of TiN crystals is a major factor, along with a change in crystal lattice orientation and texture formation, responsible for the enhancement of internal stress with coating thickening. In this context, the following remark is in order. The high level of long-range internal compressive stress ($\sigma = 4$ GPa) in nc-ZrN – Cu and the low one ($\sigma = 0.1$ GPa) in nc-AlN – Cu are related in Ref. [58] to the difference between respective grain sizes (32 and 8 nm). Meanwhile, nc-ZrN – Cu coatings reveal a similar (111) texture and columnar growth mechanism as nc-TiN – Cu. The authors of Refs [52, 53] believe that it is this fact that determines the high level of internal stresses. Specifically, an increase in the grain size in nc-AlN – Cu films to $d = 20-25$ nm does not lead to their significant enhancement compared to analogous coatings with the grain size of 8 μm [58]. Thus, the level of internal stress depends not so much on grain size proper as on the peculiarities of their fine defect substructure related to the mechanism and conditions of coating growth.

A somewhat different explanation of the properties of superhard coatings with a Vickers hardness > 40 GPa was proposed by Veprek et al. [19, 59 – 61]. These authors distinguish three approaches to the creation of superhard materials: (1) those with inner superhardness, for example, hydrogen-free diamond, diamond-like carbon (DLC), cubic boron nitrite (c-BN); (2) thin coatings in which hardness is enhanced due to a complex synergetic (?!) effect of ion bombardment during coating by plasma chemical vapor deposition (PCVD) or physical vapor deposition (PVD) methods, and (3) nanostructured superhard coatings, such as heterostructures and nanocomposites. Diamond-like carbon and polycrystalline c-BN grown at a high temperature and pressure are used extensively, whereas thin coatings obtained by PCVD and PVD have not yet found wide application.

Let us consider the fundamental difference between enhancement of hardness in heterostructures and nanocomposites, on the one hand, and in coatings strengthened by bombardment with high-energy ions, on the other hand. In 1970, Koechner [62] proposed 'construction' of durable solid materials for the formation of heterostructures. His approach is based on the prevention of dislocation movements by forming abrupt transitions (interfaces) between thin epitaxial layers. This strengthening mechanism remains valid in a situation where one of the layers is amorphous. This concept was later extended to polycrystalline structures. The reader is referred to comprehensive review papers [6, 9, 19] for details. However, we shall consider only two important issues. First, this mechanism is applicable only to crystal plasticity (active actions of dislocations). Second, sharp interfaces at the atomic level are necessary for this mechanism to operate in the case of superhard (> 40 GPa) heterostructural coatings.

Deposition of such coatings requires precise control of interfaces by means of stoppers (locks). It is rather difficult to form coatings analogous to industrially manufactured ones, i.e., multilayer coatings with diffusion across the interface instead of heterostructures; however, multilayers improve the work of coated machine components [7]. Multilayer coatings with diffuse interfaces cannot be described in the framework of Koechner's heterostructural concept.

The durability of cutting tools is usually improved by increasing fracture toughness. Hardness enhancement by ion bombardment is due to a variety of factors, viz. a decrease in crystallite size, compaction of grain boundaries, the formation of defects, and the occurrence of inbuilt bi-axial compressive stresses (according to the concept of Veprek et al. [19, 60, 61]). At the same time, residual tensile stresses may develop in the case of large ion and cluster radii compared with the size of the atoms making up the coating (see publications on ion implantation and ion beam-assisted deposition (IBAD) [178]). These effects can interfere with dislocation movements depending on crystallite size in superhard, thermally high-stable nanocomposites involving small crystallites (several nanometers) of a hard transition metal nitride (or carbide, boride, etc.), which are linked by a single thin covalent monolayer nonmetal nitride of the $Si_3N_4 : BN : CN_x$ type (the lattermost with excessive carbon).

If deposited correctly, these coatings possess an unusual combination of mechanical properties, such as high hardness (from 40 to 100 GPa), elastic recovery coefficient (from 80 to 94%), elastic stress limit (10%), and residual tensile stress (up to 40 GPa) corresponding to an 'ideal' stress in materials.

5. Superhard nanocomposites

Recent reports in the literature describe numerous superhard nanocomposites of various chemical compositions. The Ti – Si – N system appears to be the most studied. What follows will focus on this system as a model. Many researchers have studied thermodynamic phase diagrams for the Ti – Si – N system (see conclusions in Ref. [63]) and the deposition of such films by vapor-phase epitaxy (CVD) at high temperatures [64, 65]. For this reason, no hardness enhancement has been reported. Li et al. [74] were the first to make superhard Ti – Si – N films by plasma chemical vapor deposition (PCVD) method, with the use of chlorides as a source of Ti and Si [65]. Li and coworkers attributed the enhancement of hardness to the deposition of small Si_3N_4 particles within TiN nanocrystals. The maximum hardness (60 – 70 GPa) achieved by these authors was probably due to the triple nc-TiN/a-Si_3N_4/a-$TiSi_2$ structure in these coatings as confirmed later by Veprek et al. [19, 23, 96] (here, nc- and a-stand for nanocrystalline and amorphous, respectively). It is worth noting that the maximum hardness in binary nc-*Me*N/a-Si_3N_4 systems was only 50 – 60 GPa. Both Li and Veprek documented a decrease in coating hardness after a few months. They ascribed this degradation to the relatively high content of chlorine in their coatings [83]. Recent studies have shown that this is an intrinsic property of such systems attributable to chemical degradation of the $TiSi_2$ phase under the effect of air-borne water, as is the case with silicone fibers [84]. Furthermore, it became clear (after the size of the crystals had been shown to be only 3 – 4 nm) that the original explanation [65] based on dispersible hardness was incorrect. This finding promoted the development of a generalized strengthening design concept [68, 69].

Many researchers (Knotek, Andrievski, Gissler, Hammer, and some others) have described the deposition and properties of Ti – B – N coatings (see the review of these works in book [18]). It was shown in Ref. [19] that the insolubility of stoichiometric TiN and TiB_2 phases, as well as the evolution of coating morphology as a function of hardness and composition, reflect their nanocomposite nature too. The relationship between the morphology, hardness, and composition of Ti – B – N coatings was emphasized by Andrievski (see Fig. 1) in the review article [85]. The columnar structure of coatings deposited by reactive magnetron sputtering practically disappeared when their composition was such that maximum hardness amounted to $\geqslant$ 50 GPa.

Most coatings obtained by PVD at low pressures (below 10^{-3} mbar) and negative substrate potential contain high bi-axial compressive stresses (on the order of 5 – 8 GPa) in themselves as a result of bombardment with high-energy ions during deposition. It is therefore necessary to strictly exclude that the observed hardness enhancement is caused by ion bombardment. For example, the data gleaned by Hammer et al. [86] and the last report by Mitterer et al. [87] suggest a difference between hardness enhancement by ion bombardment and the formation of a stable nanocomposite structure as a result of self-organization following spinodal phase segregation. When the coatings deposited by Hammer and coworkers at room temperature were annealed at 600 – 800 °C, their hardness increased to roughly 40 GPa, and the initially amorphous films produced diffraction patterns characteristic of nanocrystals. Thus, although the TiB_2 and TiN coatings of Mitterer and coworkers show high hardness enhanced by ion bombardment during deposition, the dependence of hardness of Ti – B – N coatings on a distance corresponding to half the projective range of nitrogen ions is largely determined by the formation of the nanocomposite structure, as evident from the comparison of results reported in Refs [102, 142, 144]. A hardness maximum at a nitrogen content of roughly 27% is less pronounced than usually observed in nanocomposites deposited by PCVD method. It is likely due to an additional increase in hardness, e.g., by high-energy ion bombardment. It will be shown below that, according to the general principles of design [68, 69], such a behavior is typical of systems in which stable nanocomposites are formed. Mayrhofer et al. [66, 67] have recently presented a detailed convincing evidence of the nature of a nanocomposite with such coatings; it is also mentioned in the review [19] discussed in the present paper.

Knotek [70, 71] was the first to report the enhancement of hardness in 'superstoichiometric' TiC_{1-x} and TiC/a-C compounds [58, 59] similar to that revealed in nc-TiN/a-Si_3N_4 films with an almost 20% excess of carbon. These and related systems were later investigated by many authors (see, e.g., Refs [72, 73]). Systems bearing some analogy to TiC/a-C were later described by researchers [72, 73] who deposited multilayers of TiN and CN_x [74 – 76] or ZrN and CN_x [65] at relatively low temperatures ($\leqslant$ 200 °C). As the bi-layer thickness (period) decreased to approximately 4 nm, the hardness increased to $\sim$ 40 GPa. When the period further decreased to about 2 nm, the layered structure practically disappeared and nanocomposite morphology formed spontaneously, as shown in studies using high-resolution X-ray diffraction method and transmission electron microscopy. The nc-TiC/a-C coatings exhibit lower resistance to elevated temperatures and oxidation than nitride-based superhard nanocomposites, which restricts their use in tools for dry

and fast cutting. However, they may be useful as tribological coatings for bearings and other sliding parts due to a small coefficient of friction. Voevodin and Zabinski [72] developed a combination of TiC/C and MoS_2 coatings to be used in low-friction systems in a varying (dry/humid) medium, for example, in aircraft and space shuttle vehicles. These are but a few examples cited in the recent literature concerning Ti – B – N, TiC_{1-x}, and similar systems. In this section, we mainly focused on Ti – Si – N and related superhard nanocomposites consisting of hard nanocrystalline nitrides of transition metals and amorphous covalent nitrides, such as Si_3N_4 or BN. These nanocomposites are of special interest as having good prospects for industrial application.

6. Comparison of coatings strengthened by ion bombardment with superhard thermally stable nanocomposites

In this section, we shall compare thermally stable superhard nanocomposites with traditional coatings and composites whose hardness was enhanced by high-energy ion bombardment during deposition. Zhang et al. [77] first described this approach as probably the easiest way to obtain nitride- and boride-based superhard coatings, as well as other common hard systems including the so-called *Me*(trans)N/*Me*(2) nanocomposites comprising the hard transition metal nitride *Me*(trans)N and the soft metal *Me*(2) that does not form a stable nitride, e.g., ZrN/Ni, ZrN/Cu, Cr_2N/Ni and some others. Because later authors reported a failure of superhard nanocomposites obtained on the basis of general principle [68, 69], we shall discuss below how to distinguish between two modes of hardness enhancement under experimental conditions. One possibility is to evaluate hardness stability (measured at room temperature after each annealing step) after isochronic high-temperature annealing. Hardness enhanced by ion bombardment significantly decreases to the bulk value after annealing to 400 – 600 °C, whereas that of superhard coatings remains unaltered after annealing to 1100 °C (Fig. 10a; see also Refs [80 – 90] for an additional example). This annealing-assisted softening of superhard coatings strengthened by ion bombardment poses the main problem related to the relaxation of ion-induced film defects necessitating the enhancement of hardness during deposition [91]. In exactly the same way, the hardness of *Me*(trans)N/*Me*(2) coatings decreases as deposition temperature increases [93], the cause being thermal relaxation of ion-induced defects in the growing film at a depth greater than the ion projective range. In contrast, Veprek and Reiprich [68] reported nanocomposite hardness enhancement with a fall in deposition temperature to 500 – 600 °C. Another possibility for distinguishing between stable superhard nanocomposites and ordinary coatings is to elucidate the dependence of hardness on their composition. It should be noted that superhard nanocomposites produced according to the principle and the approach framed by Veprek and coworkers under high enough nitrogen pressure and deposition temperature [61, 68, 69, 92] possess maximum hardness (if their composition matches a percolation threshold) when the surface of titanium nitride is covered with at least one Si_3N_4 [80] or BN [89] monolayer.

Figure 10a illustrates the excellent reproducibility of the hardness enhancement process during deposition of superhard nanocomposites at high nitrogen activity (partial pressure) and temperature $\geqslant$ 500 °C as described in Refs [61, 68, 69, 92, 94]. System $TiN_{1-x}C_x$ shown in Fig. 10b is soluble over the entire composition spectrum; due to this, the mixing rule (see monograph [95], p. 391) is fulfilled, i.e., hardness grows monotonically as the carbon content increases from that in pure TiN to the ones in TiC [94]. The hardness of *Me*(trans)N/*Me*(2) coatings containing a hard transition metal nitride layer and a ductile metal [66] reaches a maximum (under the effect of high-energy ion bombardment during deposition) at a very low content of the ductile metal (see Fig. 10b). Such a behavior observed also in many *Me*(trans)N/*Me*(2) systems [93] resembles that of cemented carbide, the hardness of which also decreases with a rise in the Co content [2]. However, it remains to be proved that the presence of ductile metals (Cu, Ni, etc.) in cemented carbide also improves the fracture toughness of *Me*(trans)N/*Me*(2) coatings.

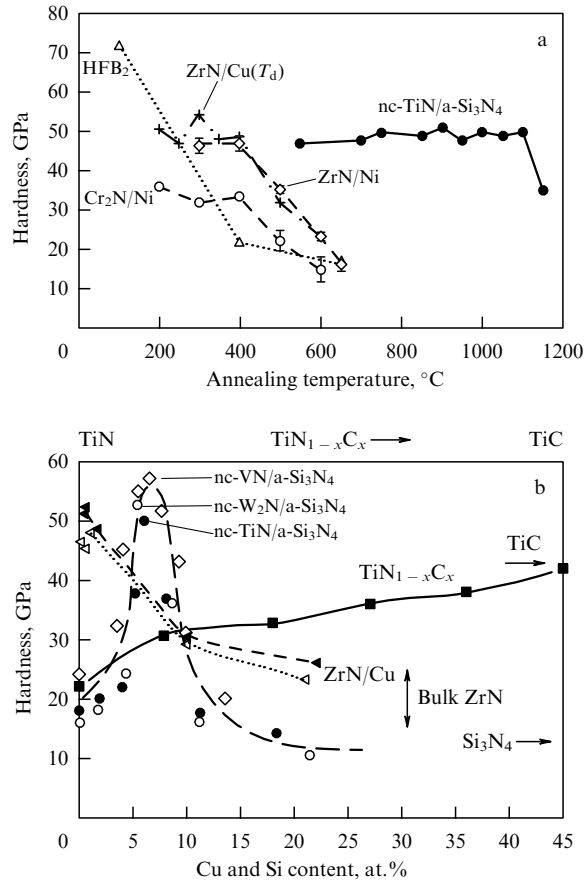

Figure 10. (a) Dependence of hardness of HFB_2 [33], Cr_2N/Ni, and ZrN/Ni [89] coatings strengthened by high-energy ion bombardment and of stable superhard nc-TiN/a-Si_3N_4 nanocomposites on isochronic annealing temperature in pure nitrogen [1, 12]. Hardness was measured at room temperature after each annealing step. Crosses show the deposition temperature dependence of ZrN/Cu hardness (Cu content slightly varied) [93]. (b) Dependence of hardness of various coatings on their composition. In a solid $TiN_{1-x}C_x$ solution, hardness obeys the mixing rule [94]. Maximum hardness of the so-called nanocomposites comprising the hard transition metal nitride and a ductile metal is achieved in the presence of the pure nitride without such a metal [93]. Superhard nanocomposites prepared following the 'design principle' formulated by Veprek and coworkers show maximum hardness at the percolation threshold [68, 69, 80].

Such a correlation between bi-axial compressive stress and hardness cannot be regarded as unambiguous evidence that hardness enhancement results exclusively (or largely)

from ion bombardment. For example, Vaz [97] and Vlček et al. [56] described a similar correlation between hardness and compressive stress for Ti–Si–N and TiN_x coatings. The question is whether the hardness of Vaz's coatings is a result of high-energy ion bombardment and/or of the formation of a nanocomposite structure. The answer is given again by the annealing experiment in which hardness of Vaz's Ti–Si–N coatings remained virtually unaltered as TiN hardness decreased under the effect of annealing [96, 98, 99]. Certain Ti–Si–N coatings produced by magnetron sputtering are liable to show 'self-strengthening' after annealing. This observation has recently been reported by Holubar et al. [100] and at greater length in Refs [88, 101] for nc-$(Ti_{1-x}Al_x)N/Si_3N_4$ nanocomposites deposited by vacuum arc evaporation. Self-strengthening is a clear evidence that the coatings were deposited under suboptimal conditions that failed to ensure the formation of thermally stable nanostructures. One example of such behavior was reported by Patscheider [102], where he very unfortunately missed the opportunity to mention a relevant earlier work. Interestingly, only one coating reported in review [102] underwent some self-strengthening, whereas the remaining ones softened after annealing to $\geqslant 500\,^{\circ}C$. Because the authors of Refs [102, 141] did not observe such a poor stability of Ti–Si–N coatings, the question arises as to the mechanism of hardness enhancement in the coatings of Patscheider and some other researchers. Similar questions will be discussed below in the context of the reproducibility of the formation of superhard nanocomposites. However, it seems appropriate to precede the discussion by expounding the concept that allows for the analysis of the properties of highly thermally stable superhard nanocomposites.

7. Conditions necessary for achieving complete phase segregation during deposition of coatings

7.1 Comparison of results

The key factor to be borne in mind when considering even a binary system is that the formation of nanostructures with high thermal stability requires a rather high chemical activity of the system to ensure the thermodynamic driving force promoting phase segregation. Moreover, a rather high temperature (500–600 °C) is required to accelerate diffusion for the completion of segregation during growth. If these conditions are not met, high hardness (50–60 GPa) in binary systems is difficult to achieve, they retain columnar morphology, and after annealing the coating may exhibit self-strengthening. Different research groups reported maximum hardness at different total Si content due to the different sizes and shapes of crystallites.

Unfortunately, most reports concerning Ti–Si–N and similar coatings do not contain information about deposition conditions and coating properties. Hence, the difficulty to elucidate the cause for the absence of data reproducibility in these works [111]. The purpose of the forthcoming discussion is to give the reader an idea of at least selected lines of research in the field of interest and to help them understand the main causes of the poor reproducibility of the results. Therefore, it will be restricted to a few typical examples.

Figure 11 illustrates the dependence of hardness on Si content for Ti–Si–N coatings formed by PCVD (Fig. 11a) and reactive sputtering (Fig. 11b) (from the data of Ref. [111]). As shown in the later work [50], the coatings obtained by Li et al. [78] were three-layered nc-TiN/a-Si_3N_4/a-$TiSi_2$ nanocomposites with hardness from 80 to $\gtrsim$100 GPa [81, 82]. It follows from Fig. 11 that the hardness of other coatings except those of Vaz [97] reached almost 40 GPa and its maxima were observable at different Si content levels. Meng et al. [103] utterly failed to document hardness enhancement in their coatings. Moreover, the hardness decreased from 32 GPa for pure TiN (correct value ca. 21 GPa [112]) to 21 GPa for Si_3N_4 (correct value ca. 17 GPa [112]). On the other hand, data reproducibility for nc-MeN/a-Si_3N_4 coatings (Me = Ti, W, V) was actually very good (Fig. 11a). It is noteworthy that these coatings were prepared by PCVD method in an intense glow discharge under a high enough nitrogen pressure ($\geqslant$ 0.5 mbar) and temperature (550 °C). According to Ref. [68], these are exactly the conditions necessary to ensure the reproducibility of characteristics of superhard films and

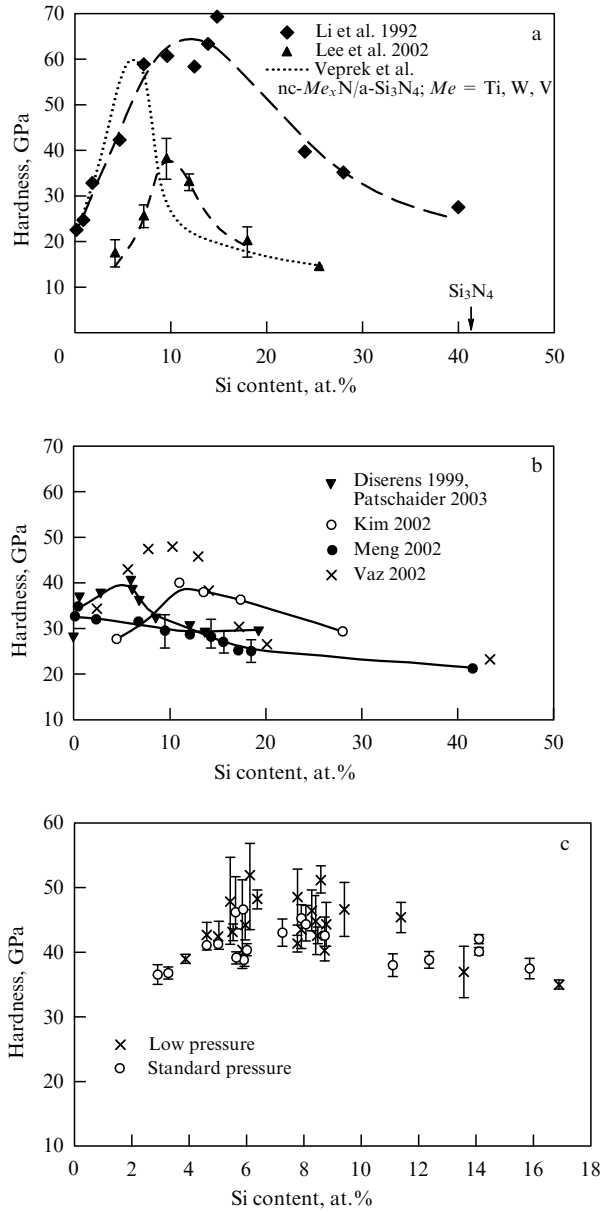

Figure 11. Hardness of nc-TiN/a-Si_3N_4 deposited by PCVD [19, 78, 105] (a) and of Ti–Si–N coatings deposited by reactive sputtering [102, 103, 106, 141] (b) depending on Si content (see also Table 2). (c) After thorough preliminary cleaning of the apparatus for film deposition (crosses).

stable nanocomposites. The films of Li and Kim [105] were deposited with coating machines similar to those in other studies but at a lower discharge current density; this accounts for the appearance of a small fraction of a $TiSi_2$ phase. The authors of Ref. [105] made use of an inductively-coupled discharge. Their results and those of experiments with glow discharges [19] indicate that this method produced the weakest of all plasmas shown in Fig. 11a. TiN nanocrystals must be covered with at least one Si_3N_4 monolayer if maximum hardness is to be achieved. Therefore, the maximum appears at a raised total content of Si, when the coating contains $TiSi_2$ in addition to Si_3N_4, as described in Refs [105, 152].

Poor reproducibility of measurements in different studies with the use of reactive sputtering and/or vacuum arc evaporation (Fig. 11c presents only a few examples) was the consequence of very low nitrogen pressure and deposition temperature, the presence of impurities, or a combination of these factors. By way of example, Meng et al. [103] used a very low partial pressure of nitrogen (0.00015 mbar) and low deposition temperature ($\leqslant 250\,^{\circ}$C). After Veprek and coworkers [108] had proposed increasing the temperature and pressure, the group led by Meng managed to enhance the nanohardness of their coatings to 38 GPa [104]. The main result of this work was formulated as "... a rise in deposition temperature from 250 to 700 °C decreased solubility of Ti in the a-SiN matrix." In other words, the researchers confirmed the data of Ref. [68] and other later studies. Nevertheless, the work [103] leaves many questions open. How does hardness change with a variation of Si content from 0 to 10 at.% as reported in Ref. [20]? Why did these researchers need such a high temperature (ca. 700 °C), while others [105, 106] reckoned 500 – 600 °C to be optimal? How reliable are hardness measurements when the maximum indentation depth is no more than 65 nm, i.e., lies within the range in which serious effects related to the scale of indentation are expected [107 – 114]? Why does the thickness of coatings "... range from 160 to 410 nm"? How low was the deposition rate, and how large was the level of impurities, especially oxygen? The very small thickness ($\leqslant 0.41$ μm) found in work [104] is a weighty piece of evidence for the very low deposition rate. Taken together with estimates reported in Section 3.1, it suggests the probability of contamination by an appreciable amount of impurity.

Similar questions arise with respect to the paper by Hu et al. [115] reporting the deposition of Ti – Si – N coatings by magnetron sputtering at a partial nitrogen pressure of 2×10^{-4} mbar (i.e., 2×10^{-7} atm). Unfortunately, the authors do not present data on the deposition rate and impurity content. A maximum hardness of 36 GPa was revealed in a single coating deposited at room temperature. Elevation of the deposition temperature to 400 °C resulted in decreased hardness (29 GPa); this fact suggests that the hardness of 36 GPa at room temperature was achieved by ion bombardment during low-temperature deposition of the layers rather than in the course of the formation of a nanocomposite. It appears that the authors chose too low a nitrogen pressure and such a composition of impurities that eventually affected the results of the study.

Hardness values reported by Vaz et al. [106] agree with those of Zhang and Veprek [61] for nc-*Me*N/a-Si_3N_4 nanocomposites obtained by PCVD (Figs 10, 11a) and reactive sputtering (see Section 7.2). A somewhat broader maximum and a shade lower hardness appear to be a consequence of the relatively low deposition temperature (400 °C) used in these experiments [106]. The hardness values thus obtained depended on the deposition temperature and substrate voltage bias (these data are presented in Fig. 11c for the optimal voltage bias −50 V; see also Ref. [146]). Maximum hardness was observed at deposition temperature close to 500 °C, in agreement with early findings [68]. It may be speculated that the coatings were not properly stabilized due to the relatively low nitrogen pressure, as follows from the appearance of a new 'phase 2' in X-ray diffraction patterns [116]; true, this phase practically disappeared after annealing. Recent studies showed that the $TiSi_2$ phase identified in these coatings by X-ray photoelectron spectroscopy (XPS) also disappeared after annealing [98]. The coating thickness being less than 3.3 μm, these hardness values appear more reliable than those reported by Meng et al. [103].

Most authors do not mention oxygen impurities, even though they may be the true cause of impaired hardness. As emphasized in the preceding section, oxygen was present inside growing coatings (up to a few atomic percent) at typical deposition rates of 0.1 – 0.5 nm s^{-1} and a residual gas pressure of $(1-7) \times 10^{-6}$ mbar. These values were reported either in papers that became available to us upon request or deduced from available information on the power and geometry of a reactor. However, it remains unclear whether the gas pressure of $(1-7) \times 10^{-6}$ mbar is a base pressure for room temperature or for deposition temperature (the two may differ by more than one order of magnitude).

The lack of reproducibility of high hardness values in a number of recent publications by other authors [102, 115] is a consequence of the wrong choice of deposition conditions (too low a nitrogen pressure and deposition temperature) and/or the presence of impurities. Incomplete information about these critical conditions in the cited papers prevents a definitive conclusion as to the dominant role of either of these two factors.

7.2 Necessary conditions for reactive sputtering

Reactive sputtering is usually conducted at lower pressures compared to PCVD, at relatively low deposition rates and

Table 2. Conditions used to deposit nc-TiN/a-Si_3N_4 nanocomposites by magnetron sputtering. Specific power at the target amounted to 15 – 18 W cm^{-2}, and deposition rate was 1.6 – 1.8 nm s^{-1}.

No. of experiment	T_{dep}, °C	Ar pressure, mbar	N_2 pressure, mbar	SiH_4 pressure, mbar	H_2 pressure, mbar	H_{max}, GPa	[Si], at.%	[O], at.%	[H], at.%
1	450 – 650	0.001 – 0.01	0.01	0 – 0.002	0 – 0.017	30	No dependence	0.4	10
2	450	—	0.02	0 – 0.002	—	30	6 – 7	2.5	2.5
3	550	0.001	0.001	Si sputtering	—	38	6 – 9	$\geqslant 0.4$	0.3
4	630	—	0.002	Si sputtering	—	45	6 – 9	0.2	0.1

frequently uses an Ar/N_2 mixture. It is therefore difficult to meet the requirements laid down in Section 7.1, when using this method. Procházka et al. [99] have recently undertaken a systematic study, the results of which are summarized in Table 2. Because sputtering of a silicon target was likely to cause cracking at high specific power, the first series of experiments were designed to deposit Ti by sputtering and introduce Si in a mixture of Si_3N_4/H_2. In later experiments, only Si_3N_4 was administered (see Table 2). Oxygen content in the coatings was 10 and $\lesssim 2$ at.% in the earlier and later series of experiments, respectively. Comparison of maximum hardness in this study with that reported in Ref. [19] indicates that hydrogen content of around 10 at.% was probably too high, since no Si-dependent increase in hardness occurred. In the second (low-hydrogen) series of experiments, the hardness increased at an Si content identical to that in PCVD-produced coatings, but its maximally achievable value was limited to 30 GPa by virtue of an elevated oxygen level.

In the third and fourth experimental series (conducted by Si sputtering) it was well established that the use of an Ar/N_2 mixture at a deposition temperature of 550 °C resulted in the oxygen admixture of 0.4 at.%, whose presence limited maximum hardness [99]. A possible cause was the release of impurities (mostly water) from the reactor walls experiencing the action of a plasma whose electric potential is always no less than 10 – 20 V and is positive with respect to any surface with which it was in contact. A large mass of argon (at an equal kinetic energy set by this voltage bias) made it more efficient than nitrogen in the release of impurities during magnetron sputtering (see Refs [117, 118] for details). Procházka [133] focused on the evaluation of the ultimate hardness attainable under reactive magnetron sputtering with the use of nitrogen alone. The very high specific power at the target and the large target – substrate area ratio in Ref. [99] made it possible to achieve a high deposition rate (1.6 – 1.8 nm s^{-1}) and obtain very thick (10 – 35 μm) and relatively pure coatings.

Figure 12a indicates that the enhanced hardness achieved in the last experimental series (see Table 2) is in excellent agreement with the dependence found earlier for PCVD-deposited nanocomposites (Fig. 10a). The maximum hardness of around 45 GPa was obviously limited by oxygen impurities. Upon the completion of the above work, the authors of Ref. [19] investigated the effect of degassing and precleaning of the coating machines and thereby managed to reduce background pressure on the substrate at the deposition temperature to 10^{-6} mbar. The crosses in Fig. 12a show that the content of oxygen impurities decreased to $\lesssim 0.2$ at.%; this led to a further increase in maximum hardness to $\gtrsim 50$ GPa.

These results clearly indicate that the maximally achievable hardness in nc-TiN/a-Si_3N_4 nanocomposites obtained by the reactive magnetron sputtering technique at a relatively high nitrogen pressure ($\geqslant 0.001$ mbar) and a deposition temperature of 550 – 650 °C depends on the oxygen impurity concentration. Higher pressure would be more advantageous but may limit the deposition rate.

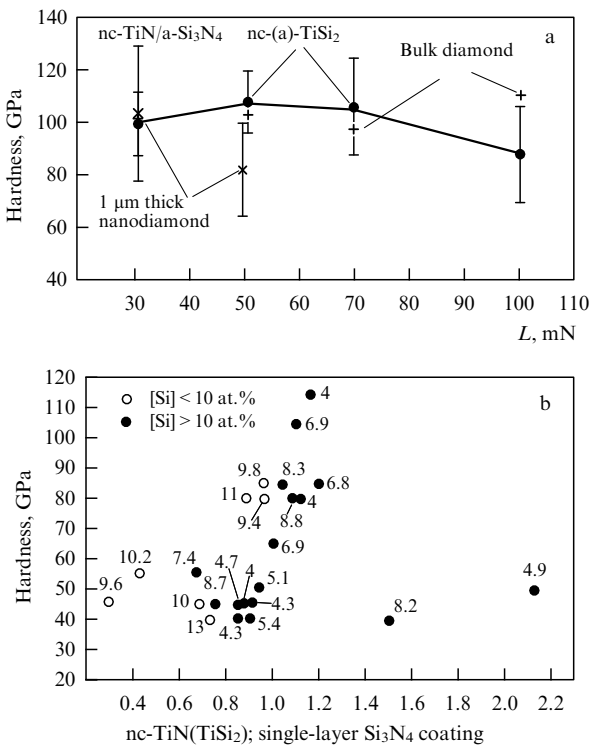

Figure 12. (a) Estimates of the load-independent hardness of the second coating, the hardest depicted in Fig. 9c, compared with bulk diamond and single-phase nanodiamond coating. At a load of 100 mN, hardness decreased because the indentation depth was 10% greater than the coating thickness of 3.5 μm. The hardness was also measured by calibrated SEM [81]. (b) Hardness of three- and four-layer nc-TiN/a-Si_3N_4/a-(nc-)$TiSi_2$ depending on the thickness of the nc-TiN coating or nc-$TiSi_2$ nanocrystals with Si_3N_4. Arabic numerals denote the size of crystallites.

8. Superhard (80 – 100 GPa) coatings

Up to now, a superhardness of 70 – 80 GPa has been achieved only in three-layer nc-TiN/a-Si_3N_4/a-$TiSi_2$ [78, 80 – 82], and of 100 GPa in four-layer nc-TiN/a-Si_3N_4/a-$TiSi_2$/nc-$TiSi_2$ [80, 81] at an oxygen content below 0.07 at.% (see Ref. [82], p. 155). Fears that such a high hardness could be a result of measuring error [119] were dismissed as irrational by the results of Ref. [120]. In an earlier study, these estimates were compared with the data for a bulk diamond single crystal as illustrated in Fig. 12a. It can be seen that superhard coatings evidence a load-invariant hardness of 100 GPa that slightly decreases at a maximum load of 100 mN when the indentation depth reaches about 17% of the coating thickness (3.5 μm). A hardness of 91 GPa obtained under such a load was verified both by measuring the residual plastic deformation area with calibrated scanning microscopy and by computation [121]. It was shown that the load-invariant hardness of nanocomposite coatings is in excellent agreement with bulk diamond hardness within the entire 30 – 70 mN range and with the hardness of single-phase nanocrystalline diamond at a small load.

The self-consistency of these data was checked by Argon and Veprek [122, 123] based on the universal binding energy relation (UBER) [124 – 125] and the Herzian analysis for indentation measurements [2, 107, 108]. Veprek and co-workers concluded that the aforementioned high values of hardness had been measured correctly. It follows from work [80] that both a high purity and an adequate composition of Si-containing phases are needed for a reproducible coating deposition. Similar to the systems composed of other materials, maximum hardness is achieved when a TiN nanocrystal surface is covered with at least one Si_3N_4 monolayer. Although the reproducibility of deposition of

these nanocomposites is more difficult to reach compared with binary coatings, the hardness exceeding 80 GPa was possible to reproduce in more than 15 coatings; a value of $\gtrsim 100$ GPa was achieved in six other cases [120].

High hardness was initially attributed to the presence of a $TiSi_2$ phase. However, the strong dependence of hardness on oxygen impurities (at the content below 0.1 at.%) poses the question of whether $TiSi_2$ acts as a trap for these impurities and prevents their accumulation at the TiN/Si_3N_4 interface. In-depth studies are needed to answer this question.

The above coatings are of interest due to the possibility of obtaining materials harder than diamond. From the practical point of view, $TiSi_2$-containing coatings have a disadvantage related to the instability of this phase after long-term exposure to the air (see Section 7.1). Impairment of hardness in coatings studied by Li et al. [78] after exposure for a few months was first ascribed to their relatively high chlorine content. However, the hardness of ultrahard nc-TiN/a-Si_3N_4/a-(nc-)$TiSi_2$ coatings also decreased after a 6 – 8-month-long exposure, despite their lower chlorine content (usually < 0.5 at.%) [19]. The researchers explained this instability by that of silicon titanate forming several phases with different stoichiometry, such as Ti_5Si_3, TiSi, and $TiSi_2$ (the last being most stable) [125, 126]. However, experiments at relatively low temperatures (500 – 600 °C) yielded metastable $TiSi_2$ phases [82] further transformed to stable ones [87] only at high temperatures. Because this phase transition was kinetically confined to a small volume, $TiSi_2$ nanocomposite coatings were susceptible to a chemical attack for the part of polar water molecules [125, 126]. This situation is reminiscent of that with silicon fibers, in which an ideal tensile stress of 24 GPa can develop immediately after preparation. True, their hardness rapidly decreases in the moist air due to microcracking (see monograph [84], p. 172), falling to 0.3 GPa within 24 hours.

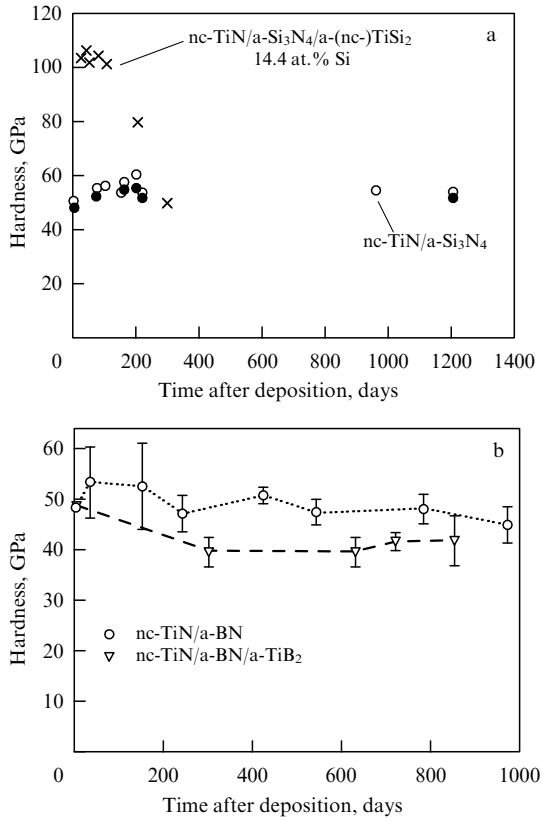

Figure 13. Long-term stability of nc-TiN/a-Si_3N_4 and nc-TiN/a-Si_3N_4/a-(nc-)$TiSi_2$ (a), and nc-TiN/a-BN/a-TiB_2 (b) after exposure at room temperature in the laboratory conditions. Air humidity was not monitored.

9. Properties of superhard coatings

9.1 Long-term stability in the air at room temperature

As noted in the preceding section, ultrahard three-layer and four-layer nanocomposites are vulnerable to degradation during long-term exposure to the air. However, binary superhard nanocomposites, such as nc-TiN/a-Si_3N_4 and nc-TiN/a-BN (as well as nc-TiN/a-BN/a-TiB_2), remain stable after exposure for a few years (see Fig. 13). It should be noted that the stability of several coatings in each system was evaluated for a long period, but only one example is presented in Fig. 13. As mentioned in the previous section, the hardness of ultrahard nc-TiN/a-Si_3N_4/a-(nc-)$TiSi_2$ decreased within a few months after the onset of exposure to the air (Fig. 13a).

Suzuki et al. [127] observed disintegration of $(Ti_{0.33}Al_{0.67})N$ coatings with a face-centred cubic (fcc) lattice and near-limit metastable solubility into a fcc-TiN and h-AlN hexagonal structure after a year-long exposure to the air. The coatings were prepared by IBAD. Because these coatings find industrial applications, Veprek and coworkers (see the respective reference in work [19]) examined a series of such materials of typical composition $(Ti_{0.40}Al_{0.60})N$ used in the manufacture of cutting tools. They were produced by vacuum arc evaporation in an industrial coating machine (PLATIT, Sweden jointly with SHM, Czech Republic). After the failure to observe any disintegration or softening in the air, the authors of Ref. [19] undertook a series of 'rapid' tests in which one part of the coatings were stored in an atmosphere of nitrogen at 300 °C, and the other in the air at 100% humidity at 70 – 80 °C. Even in these conditions, no signs of decomposition or softening could be recorded after a 9-h exposure. This is actually an important finding, but the question remains as to why the coatings prepared by Suzuki and coworkers underwent degradation? One explanation may be the relatively high oxygen content (ca. 10 at.%) in those coatings or too high a content of Al close to the metastable solubility limit [127].

Bull and Hainsworth [128] found that the hardness of DLC coatings deposited by high-energy ion bombardment decreased after long-term storage; the authors accounted for this reduction by relaxation of the high bi-axial compressive stresses initially present in the coatings. A hardness of 80 GPa was reported by Héau and Terrat [129] for Ti – B – N coatings deposited by combined magnetron sputtering from Ti and TiB_2 targets; the coatings contained 13 at.% B, 37 at.% Ti, and 50 at.% N. Their hardness decreased to 46 GPa after a few days of storage in the air. ZrN/Ni coatings made superhard by ion bombardment also underwent reduction of hardness after storage for 1 year at room temperature. Impairment of hardness was repeatedly recorded in all seven ZrN/Ni coatings containing from 0.46 to 4.1 at.% Ni. Such a limited stability at room temperature should be borne in mind when considering potential areas of application of coatings strengthened by bombardment with high-energy ions.

9.2 Thermal stability and self-hardening of nanocomposites

The thermal stability of thin nitride films (grown largely by PVD) has been discussed in a recent review by Hultman [91]. We are focused here on thermal stability and self-strengthening of nanocomposites because polycrystals having a fine-grain structure undergo recrystallization at annealing temperatures exceeding $0.4T_m$ (T_m is the melting point, K; such recrystallization is referred to as 'Oswald ripening' [130, 131]). So high thermal stability as shown for nc-TiN/a-Si_3N_4 nanocomposites in Fig. 10a is rather surprising because Oswald ripening is thermodynamically supported by an excess (destabilizing) contribution of surface (or grain boundary) energy to the total Gibbs free energy; in other words, large crystallites grow at the expense of smaller ones. High thermal stability and oxidation resistance were already described in the earlier work [68] and later studied in greater detail in Refs [88, 94].

Selected examples of the thermal stability of different coatings are presented in Fig. 14. One of the many nc-TiN/a-Si_3N_4 coatings (see Fig. 14a) was formed by PCVD in an intense discharge at a nitrogen pressure of $\geqslant 0.3$ mbar and temperature of 550 °C [68, 88, 132]. It should be noted that this coating was annealed at a 'basic gas' pressure of 10 mbar (90% N_2 + 10% H_2), while coatings in Fig. 14b, c were annealed under a pressure of N_2 of 1 atm. Figure 14b presents the results for a coating of nc-TiN/a-Si_3N_4 deposited by reactive magnetron sputtering under near-optimal conditions ($P_{N_2}/P_{Ar} = 1$, $P_t = 2 \times 10^{-3}$ mbar, $T_s = 550$ °C, a deposition rate of 1.8 nm s^{-1}) [99]. Notice that the hardness of coatings deposited by PVD under optimal conditions was above 50 GPa [132–135]. Figure 14c presents data on nc-TiN/a-BN deposited by PCVD under roughly the same conditions as nc-TiN/a-Si_3N_4 in Fig. 14a, where BCl_3 was used instead of SiH_4 [136]. The coatings in Fig. 14a, c were deposited onto silicon (100) substrates to avoid diffusion of metals from steel, Mo, and other metal substrates. Such diffusion starts at above 900 °C, promotes recrystallization, and in the end impairs hardness [133–135].

It can be seen that both crystallite size and coating hardness are stable up to 1100 °C for nc-TiN/a-Si_3N_4, and up to 1000 °C for nc-TiN/a-BN. The slightly lower stability of nc-TiN/a-BN is a result of partial BN oxidation by residual oxygen in the atmosphere of N_2 (99.999% purity) and the loss of boron in BO_x sublimation, as shown earlier in Refs [134, 137]. The highest thermal stability of nc-TiN/a-BN nanocomposites is reached in the case of its optimal composition, i.e., when TiN nanocrystals are covered with approximately one BN monolayer [136, 137]. This case is different from that of nc-TiN/a-Si_3N_4, in which thermal stability remains high despite supraoptimal Si_3N_4 content. The difference in the behaviors of these two systems is due to the higher oxidation resistance of Si_3N_4 compared with BN. We regard the temperature of 1100 °C (the limiting temperature at which nitrogen saturation pressure reaches 1 atm [138]) as the stability limit for nc-TiN/a-Si_3N_4 coatings. This temperature is much higher than that near $0.4T_m$ where Oswald ripening occurs. Its absence may be a consequence either of slow diffusion at low temperature or of the lack of reaction at the interface (i.e., the insolubility of the two phases at a high temperature [83]). In earlier studies, the low diffusion coefficient limit (necessary when the absence of Oswald ripening at 1000 °C resulted from too low a diffusion rate) was determined as $D \leqslant 10^{-20}$ cm^2 s^{-1} (see paper [132], p. 145). It was confirmed in Ref. [132] that this value should be one order of magnitude smaller than any reasonably expected one (see paper [91] for a comparison). Therefore, the high thermal stability of these nanocomposites is unrelated to slow diffusion. Evidently, it is due to the lack of reaction at the interface [130], i.e., to the expressed insolubility of stoichiometric TiN and Si_3N_4 phases. Expressed insolubility is consistent with the spinodal nature of phase segregation.

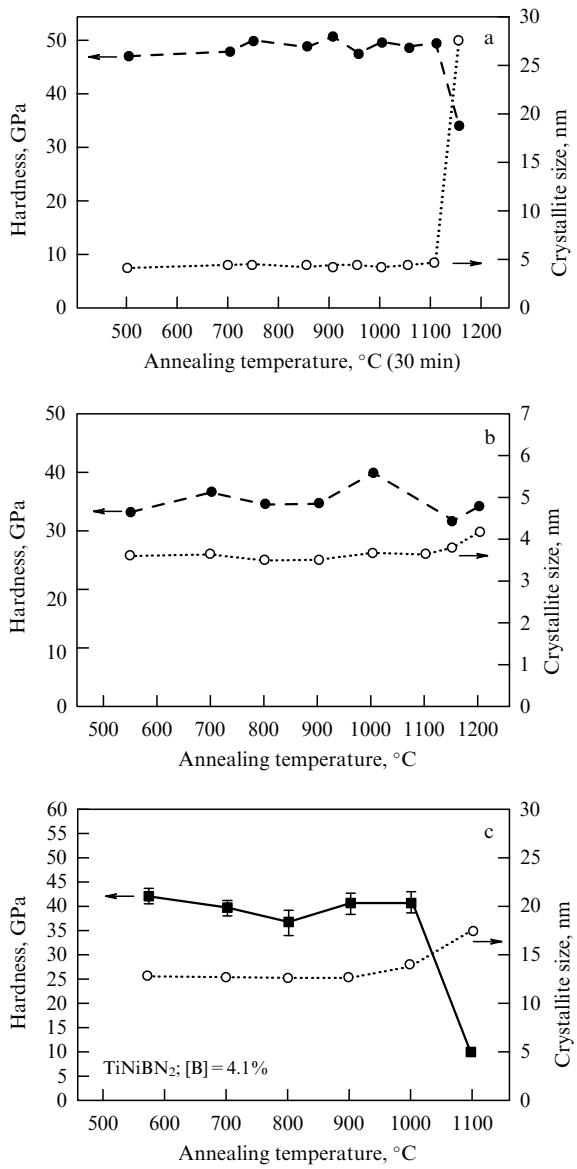

Figure 14. Thermal stability (isochronic annealing in pure N_2 or the basic gas for 30 min at each temperature): (a) nc-TiN/a-Si_3N_4 deposited by PCVD on an Si substrate with a thick TiN layer at the interface [68, 88, 132]; (b) nc-TiN/a-Si_3N_4 deposited on a molybdenum substrate by magnetron sputtering under near-optimal conditions [99], and (c) nc-TiN/a-BN deposited by PCVD on an Si substrate [142, 151].

Self-strengthening phenomenon, i.e., hardness enhancement after annealing, was described by Holubar et al. [100] for coatings nc-$(Al_{1-x}Ti_x)N$/a-Si_3N_4 deposited onto an industrial specimen by vacuum arc evaporation at a nitrogen pressure of 2×10^{-3} mbar and a temperature of 550 °C. Figure 15b exemplifies such behavior based on the results of Veprek from the joint study with the Holubar group using nanocomposites nc-$(Al_{1-x}Ti_x)N$/a-Si_3N_4 deposited onto a

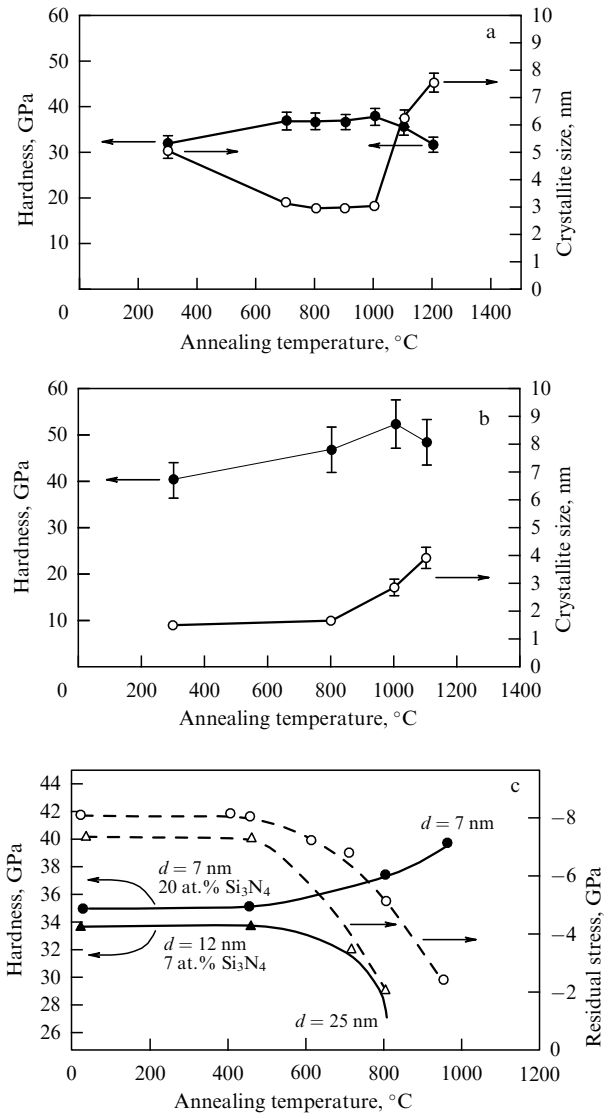

Figure 15. Self-strengthening and the associated change in crystallite size to 3 – 4 nm after annealing of nc-$(Al_{1-x}Ti_x)N$/a-Si_3N_4 deposited under far-from-optimal conditions (white circles) that yielded too large crystallites (high temperature, bombardment with low-energy ions) (a) or too small ones (low temperature, bombardment with low-energy ions [101, 139]) (b); black circles in Fig. 15a,b correspond to optimal deposition conditions. (c) Annealing behavior of Ti – Si – N coatings obtained by Patscheider [102] by reactive sputtering method. The denotation 'at.% Si_3N_4' is borrowed from review [102]; the author appears to have meant 'mol.%'.

substrate at different temperatures and bias voltages [101, 139]. It should be noted that the coating reached an 'optimal' thickness of 3 – 4 nm regardless of the primary size of the crystallites after deposition. This observation refers to all nc-*Me*N/a-Si_3N_4 coatings grown by PCVD in an intense discharge under conditions facilitating the complete formation of a stable nanostructure during deposition. It may be concluded that self-strengthening is typical of incomplete phase segregation following deposition; as emphasized by Gahn [140], it takes place as a result of post-annealing phase segregation. Such thermal stability of nanocomposites is due to the fact that the final, fully segregated nc-TiN/a-Si_3N_4 nanostructure corresponds to the final stage of spinodal segregation of stoichiometric phases. Simple thermodynamic considerations [63, 69, 135] imply that the same conclusion holds for a series of nc-*Me*N/a-Si_3N_4, nc-*Me*N/a-BN coatings, and other systems. In this context, the strengthening design concept [68] is of paramount importance.

The results of studies on the thermal stability of nanocomposites were published later by several research groups. As far as the system of Ti – B – N is concerned, the authors refer to Fig. 14c and the last works by Mayrhofer and coworkers (see Refs [66, 67] and references cited therein). A typical example of this system deposited in undue conditions is presented in Fig. 15c based on the data of Patscheider [102]. The figure shows that annealing of coatings containing 7 at.% Si_3N_4 (what is meant is probably 'mol.% Si_3N_4' or 'at.% Si') to $\geqslant 500\,^\circ$C leads to a significant increase in hardness and compressive stress. A simultaneous decrease in hardness and compressive strength (from $\gtrsim -7$ to -2 GPa), along with comparison to the behavior of coatings strengthened by high-energy ion bombardment (Fig. 13a), indicates that the average enhancement of hardness (34 GPa) shown in Fig. 15c may just as well result from the effect of ion bombardment. The authors of paper [19] failed to observe such low thermal stability in any nc-TiN/a-Si_3N_4 specimen deposited under conditions facilitating the formation of a stable nanostructure. Deposition conditions for Ti – Si – N in Refs [141, 142] are not specified and the thesis of M Diserens referred to in Ref. [102] (see Ref. [30] in review [102]) was unavailable at the time of writing the present review. It may be conjectured that these conditions were similar to those used in an earlier work by the same authors, where temperature "was never higher than 350 °C", surface bias voltage ranged between -100 and -125 V, and "variation of Si content (in the coating) was achieved by using a different partial pressure of nitrogen which varied from 8×10^{-2} to 1.2×10^{-1} Pa" (0.0008 – 0.0012 mbar) at "the base pressure in the reactor below 2×10^{-4} Pa" (2×10^{-6} mbar, see Ref. [141]). The same information about the deposition conditions can be found in other publications by this group [73, 141 – 144]. Comparison of deposition conditions from many works in which the hardness of coatings was enhanced by ion bombardment shows that the conditions used by Patscheider and coworkers were typical of strengthening by this method. It is therefore understandable why their Ti – Si – N coatings behaved very similarly unlike those with nearly the same Si content in the experiments by Veprek et al. [62].

Moderate self-strengthening observed in coatings with a high content of Si_3N_4 (on the order of 20 at.%; see Fig. 15) is probably related to the phase segregation considered above. All nc-*Me*N/a-Si_3N_4 coatings demonstrating maximum hardness and remaining stable after annealing to 1100 °C (Fig. 14a, b) contained roughly 20 at.% Si_3N_4. This comparison once again confirms that deposition conditions and the resulting nanostructure of Ti – Si – N coatings reported in paper [19] were far from optimal. Unfortunately, we cannot discuss possible causes in greater detail for lack of comprehensive data on the composition (20 at.% Si or mol.% Si_3N_4?), deposition conditions, impurity content, and other characteristics in the papers of Patscheider, who does not even refer in his reviews [73, 102] to similar or more accurate data obtained by earlier authors.

Mayrhofer et al. [145] have recently reported transient self-strengthening after an initial stage of the decomposition of $(Ti_{1-x}Al_x)N$, which proceeds through the formation of an intermediate metastable cubic phase (c-AlN) at about 800 – 900 °C. This stage resulted from spinodal decomposition of a supersaturated solid $(Ti_{1-x}Al_x)N$ solution at the surface of

fcc TiN crystals. Further annealing to > 900 °C decomposed the solution to h-AlN and softened the covering.

The results obtained by Bull et al. [111] suggest an almost heteroepitaxial growth of an Si_3N_4 layer at the TiN surface. It is expected that such a configuration will be highly stable [145]; it is considered to be the most likely cause of the excessively high thermal stability of nc-$(Al_{1-x}Ti_x)N$/a-Si_3N_4 coatings obtained in work [139]. Recrystallization and softening stop at 1200 °C revealing strong cobalt diffusion from the cemented carbide substrate after annealing [139]. This means that the thermal stability of $(Al_{1-x}Ti_x)N$-coated articles is limited by that of cemented carbide.

9.3 Oxidation resistance

The high oxidation resistance of superhard nc-TiN/a-Si_3N_4 nanocomposites having an optimal composition and hardness exceeding 50 GPa was considered in the first work by Vepřek and Reiprich [68]. Figure 16a borrowed from Ref. [94] compares the thermal stability of PCVD-formed nc-TiN/a-Si_3N_4 [68] with a variety of industrial coatings as reported by Münz in 1986 [146]. Thermal stabilization was applied to yttrium-doped (TiAl)N coatings [147, 148]. Figure 16b demonstrates the oxidation resistance of PCVD-formed superhard nanocomposites nc-TiN/a-BN and superhard nanocomposites nc-TiN/a-Si_3N_4 deposited by magnetron sputtering under conditions that ensured the development of a stable nanostructure [99, 133].

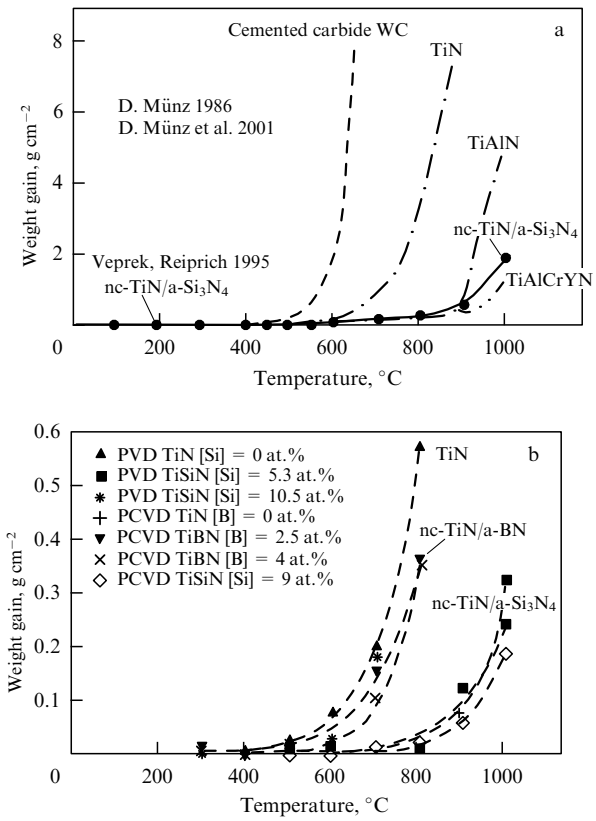

Figure 16. (a) Oxidation resistance of PCVD-deposited nc-TiN/a-Si_3N_4 nanocomposites [8] compared with other industrial hard coatings [19, 94]. Data on oxidation resistance of WC, TiN, and $(Ti_{1-x}Al_x)N$ coatings were borrowed from Ref. [146], and of TiAlCrYN from Refs [147, 148]. (b) Oxidation resistance of PCVD-deposited superhard nc-TiN/a-BN nanocomposites [134, 147] and of nc-TiN/a-Si_3N_4 deposited by magnetron sputtering under conditions ensuring formation of a stable nanostructure [99, 133].

The oxidation resistance of stable and superhard nc-TiN/a-Si_3N_4 nanocomposites with a maximum hardness of 50 GPa [68] is compared with that of yttrium-doped $(Al_{1-x-y}Ti_xY_y)N$. The stability of superhard nc-TiN/a-BN nanocomposites is slightly higher than that of TiN but not much better in comparison with nc-TiN/a-Si_3N_4. High oxidation resistance in the last nanocomposite is due to the strong and dense Si_3N_4 interface that hinders oxygen diffusion along grain boundaries (note that yttrium in $(Al_{1-x-y}Ti_xY_y)N$ also interferes with oxygen diffusion along grain boundaries). The lower stability of nc-TiN/a-BN is a result of the lower oxidation resistance of the BN phase as shown in papers [136, 137] reporting the loss of boron after oxidation due to reoxidation and sublimation of BO_x suboxides.

The lower oxidation resistance of TiN is also known from the works by Münz and coworkers [146–148], while the enhanced oxidation resistance of Si_3N_4 is thoroughly described in textbooks. Similar to SiC, Si_3N_4 develops a dense SiO_2 layer under the effect of oxidation that prevents oxygen diffusion up to high temperatures of about 1600 °C. On the other hand, the low melting point of B_2O_3 (450 °C) [138] determines the reduced oxidation resistance of the BN phase. It accounts for the enhanced oxidation resistance of nc-TiN/a-Si_3N_4 coatings with a rise in Si_3N_4 content, although their hardness decreases after this content increases to values above 20 vol.% [68, 94]. At the same time, there is no apparent relationship between oxidation resistance and BN content in the case of nc-TiN/a-BN coatings (see Ref. [136] for details).

Improved oxidation resistance of Ti–Si–N coatings in comparison with TiN was later reported by several research groups, e.g., in paper [141] and in the review by Patscheider [102]. However, these publications contained no new interesting data and/or interpretations compared with earlier studies cited in the present article. The formation of nc-$(Al_{1-x}Ti_x)N$/a-Si_3N_4 also improves the oxidation resistance of nanocomposites in comparison with $(Al_{1-x}Ti_x)N$. It is little wonder, because when the Si_3N_4 phase stabilizes and protects $(Al_{1-x}Ti_x)N$ against disintegration and softening, it remains stable and dense; the same is true of interfaces. Worth noting is the result of Tanaka et al. [149], who described a substantial improvement of oxidation resistance in (TiAlSi)N coatings compared with (AlTi)N, although according to their analysis these materials were not nanocomposites but solid solutions of Si in the (AlTi)N phase (see paper [149] for more details). As mentioned above, coatings have a lower hardness than superhard nanocomposites, although their oxidation resistance and cutting parameters were significantly improved only in comparison with $(Al_{1-x}Ti_x)N$ [149].

9.4 Morphology and microstructure

The development of the columnar morphology of PCVD and PVD coatings prepared at relatively low temperatures (300–600 °C) is described by Thornton's structure–zone diagram (see handbook [150], p. 712). This diagram is an extension of the Movchan–Demchisin structure–zone diagram for films obtainable by gas-phase epitaxy (see Ref. [150], p. 711). A proper combination of homologous temperature $T_h = T/T_m$ (T is the deposition temperature, T_m is the melting temperature of a given material, K) and energy transferred by ions toward the growing film surface on a deposited atom basis permits obtaining coatings within the so-called 'T-zone' corresponding to a columnar but relatively dense structure.

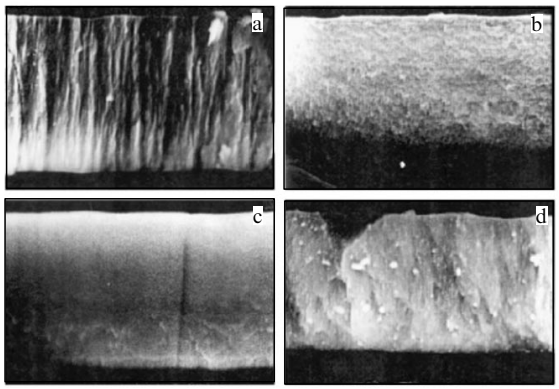

Figure 17. (a) A cross section through TiN coatings with a columnar structure obtained by PCVD from $TiCl_4$, SiH_4 with an excess of N_2 and H_2 at 550 °C; (b) nc-TiN/a-Si_3N_4 nanocomposites containing 5 at.% Si and having a hardness of ca. 35 GPa (Fig. 7a); (c) nc-TiN/a-Si_3N_4 nanocomposites with an optimal Si content (7 – 8 at.%) and stable nanostructure (hardness of about 50 GPa), and (d) nc-TiN/a-Si_3N_4 nanocomposites with a too high content of Si (ca. 9 at.%) and a hardness of 30 GPa (taken from Ref. [9]).

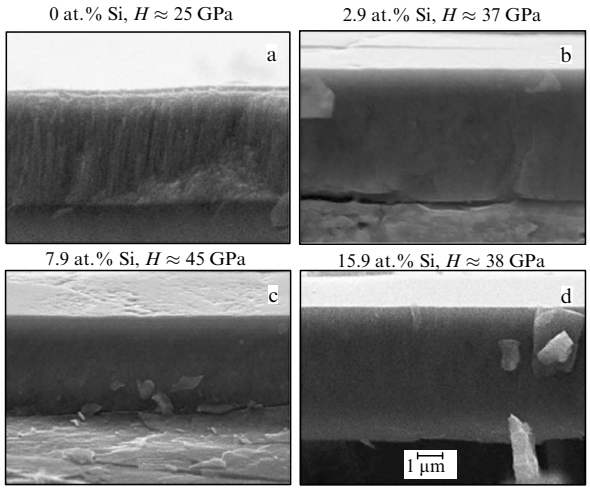

Figure 18. Development of nc-TiN/a-Si_3N_4 morphology after magnetron sputtering with growing Si content.

The columnar structure practically disappears when superhard nanocomposites of optimal composition are formed. This was shown by Li et al. [78] as early as 1992 for PCVD-formed Ti – Si – N films and later confirmed in the works by Veprek and coworkers for other binary nanocomposites nc-*Me*N/a-Si_3N_4 (where *Me* = Ti, W, V) obtained by PCVD in an intense discharge [69]. Figure 17 depicts the morphological development of nc-TiN/a-Si_3N_4 after the addition of Si (notice that in all these coatings, silicon is present in the form of Si_3N_4 with lacking contribution from the $TiSi_2$ phase) [68]). The TiN columnar structure (Fig. 17a) and surface morphology are isotropic at elevated Si_3N_4 content and correspond to optimal composition and maximum hardness (Fig. 17c). It should be noted that coatings deposited onto Si substrates as described in Ref. [100] cracked, whereupon microdiagrams had to be taken without polishing the surfaces. The morphology remained unaltered after a further rise in Si_3N_4 content, but hardness again decreased (Fig. 17d). A similar behavior was described in Ref. [69] for nc-W_2N/a-Si_3N_4 and many other nanocomposites (nc-VN/a-Si_3N_4, nc-TiN/a-Si_3N_4/a-(nc-)$TiSi_2$, nc-$(Al_{1-x}Ti_x)N$/a-Si_3N_4), but the results were not published due to the lack of novelty (in opinion of Veprek et al.). Figure 18 illustrates a very similar development of nc-TiN/a-Si_3N_4 morphology after magnetron sputtering (see Fig. 12a and the above discussion). Despite the isotropic morphology of nanocomposites with maximum hardness deposited by magnetron sputtering, an in-depth TEM study revealed their partially columnar, even if rather dense, structure [151]. It may be a consequence of relatively low nitrogen pressure which precludes completion of the nanostructure formation. Further investigations are needed to better understand this problem.

The dense and isotropic nanostructure developing after formation of a stable superhard nanocomposite even within the dense T-zone is far from 'ideal' in terms of mechanical properties by virtue of weak intercolumnar links. Hence, the columnar morphology of PCVD nanocomposites needs to be eliminated altogether if materials with excellent mechanical characteristics are to be produced. The universal dependence of morphology on the formation of stable superhard nanocomposites is confirmed by earlier reports on identical isotropic structures in nc-TiN/a-BN and nc-TiN/a-BN/a-TiB_2 coatings [136]. Certain research groups reproduced these data and thereby confirmed them to a degree [152, 153]. However, results of scanning electron microscopy (SEM) presented in these publications indicate that coatings retain well-apparent columnar morphology even after the addition of silicon [102, 153, 154, 115]. This can probably be accounted for by the fact that all these authors used a lower partial pressure of nitrogen than Procházka et al. [99].

The authors of Refs [115, 155] also discuss mechanisms governing the aforementioned morphological changes but totally disregard the phase segregation concept formulated a few years ago [68, 69]. For example, Patscheider et al. [143] postulate a certain type of nonspecific 'renucleation' of TiN grains following "partial deposition of Si_3N_4 onto TiN". The authors do not even refer to the thermodynamic and kinetic considerations presented in Refs [68, 69], nor do they go into the details of the renucleation mechanism that regulates morphological development. However, SEM micrograms presented in Refs [68, 69] show that their Si-containing coatings (12 at.%) with a maximum hardness around 40 GPa [73, 102, 141 – 143] obviously retained a well-apparent columnar structure [142].

Hu et al. [115] also revealed a similar tendency; in their study, a rise in Si content from 0 (pure TiN) to 5 at.% did not result in the disappearance of columnar morphology. The present authors conclude that speculative arguments in Ref. [115] fully ignore the thermodynamic and kinetic data reported over 10 years ago by Vepřek et al. [68, 69]. The results of Hu and coworkers are easy to understand taking into account the hardness values presented in their paper. Maximum hardness (ca. 36 GPa) was obtained only for coatings with 4 at.% Si deposited at room temperature; those prepared at 400 °C had their maximum hardness reduced to 28 GPa. This means that hardness enhancement in coatings deposited at room temperature is first and foremost a result of bombardment with high-energy particles always present in magnetron sputtering at low gas pressures due to the reflection of primary ions from the target. Base pressure in the system employed by Hu et al. was 10^{-6} mbar,

and partial nitrogen pressure 2×10^{-4} mbar. The authors interpreted this fact as suggesting the presence of silicon, not only in the form of Si_3N_4 but also as Si (true, the critically disposed reader will notice that the Si 2p XPS signal ascribed by the researchers to elemental Si might just as well originate from $TiSi_2$). Collectively, these results indicate that coatings of Hu et al. and Patscheider et al. were deposited under improper conditions that prevented formation of a stable fully segregated nanostructure during film growth and accounted for prevailing columnar morphology, even if less pronounced.

Many authors reporting a different type of behavior of hardness, morphology, and other properties suggest alternative interpretations. However, it is difficult to analyze these works for the lack of the comprehensive characteristics of deposition conditions and/or test samples and due to the necessity of excluding injurious effects of impurities. By way of example, Jiang et al. [176] prepared a series of Ti–Si–N coatings at room temperature by unbalanced reactive magnetron sputtering at an overall (Ar $+N_2$) pressure of 2.6×10^{-3} mbar but did not specify the partial nitrogen pressure. Hence, no wonder that only part of the augmented amount of silicon in the coatings was involved in the formation of the Si_3N_4 type linkage but the remaining Si 'did not participate in the reaction', while columnar morphology was preserved (see Ref. [176]). The small thickness of the coatings (within 1 μm) [176] necessitated hardness measurement at low pressure and maximum indentation depth ($\lesssim$80 nm). The results of these measurements need thorough verification, bearing in mind the possible indentation size effect (ISE) which is able to adulterate them. The authors of Ref. [176] observed hardness enhancement to 35 GPa when Si content ranged 8–10 at.%. However, the presence of oxygen impurities (5–8 at.%) [176, p. 169] makes this work of little value for understanding systems of this kind. Such criticism equally applies to many other studies where coatings were deposited "... without applying substrate bias voltage or heating, for the evaluation of the added silicon effect alone..." [156]. A rise in deposition temperature to 300 °C and application of −100 V bias voltage [154] led to hardness enhancement unrelated to bombardment with high-energy ions or correlation between hardness and compressive stress.

10. Mechanical properties of superhard nanocomposites

Understanding of extraordinary mechanical properties of nanocomposites was initially based on the absence of dislocation activity in small (a few nanometers) crystallites, a very low stress level for small ($\lesssim$1 nm) nanocracks, and the resulting necessity of high stresses for crack initiation and propagation in the systems lacking grain boundary sliding [61, 68, 69, 80, 94, 132]. Well-defined interfaces between nanocrystals and the Si_3N_4 phase were attributed to thermodynamically governed phase segregation. This situation is critically different from nanocrystalline materials obtained by means of consolidation, when the grain boundary sliding is impeded [157–162]. The important contribution brought about by Argon's studies [122, 123, 163, 164] provided a significantly deeper insight into the problem. It was shown that the mechanical properties of nanocrystallites are easy to explain in terms of conventional fracture mechanics, taking account of their nanometer scale and an amorphous covalent transition silicon nitride one monolayer thick, when these materials have no cracks. This situation is due to the formation of a stable nanostructure by self-organization during spinodal phase segregation. Our discussion is confined to a brief summary of earlier publications on this problem.

Plastic deformation of ductile materials like metals proceeds via dislocation activity or shift transformations, such as deformation twins or martensitic transformations [95, 163]. Plastic flow in glasslike solids, for example, amorphous metals, occurs as shift transformations return to bulk ferrite elements where they are 3–4 nm in size [164]. A recently developed molecular-dynamic Si-glass model implies that localized plastic deformation in covalent amorphous solids is triggered by simultaneous collective movements of 5–6 atoms. Redistributed clusters under plastic deformation contain 100–500 atoms [165]. Plastic deformation evolving by any of these mechanisms requires a finite activation volume [163, 165–167]. This situation resembles that of structure-phase transformations resulting from imposing pressure to nanometer-sized single crystals, where transition pressure increases with decreasing crystal size. Reverse transition after unloading is characterized by hysteresislike enhancement upon a decrease in the crystallite size [168]. Plastic deformation is utterly impossible to induce within nanometer-sized crystallites and a single Si_3N_4 monolayer or BN 'glue' in stable superhard nanocomposites, the strength of which might afterwards reach an 'ideal' level.

Such an ideal strength of perfect solids (crystals or glasses) is characterized by decohesion energy $\sigma_c \approx (E\gamma_s/a_0)^{0.5}$ (E is the Young modulus, γ_s is the surface energy, and a_0 is the interatomic bond length; see Ref. [95], p. 239). Calculations based on this relation give an ideal strength of solids on the order of 20–50 GPa, close to its observed values in freshly prepared glass fibers. Indeed, tensile stress in freshly prepared SiO_2 fiberglass amounts to 24 GPa or 25% of the Young modulus (see Ref. [71] p. 240). Elastic stress for ideal solid matter recovery can be as high as 20% (see monograph [95], p. 239; Refs [92, 107] and references cited therein).

Based on the universal binding energy relation (UBER) [124, 120], Argon and Veprek [122] assessed the ideal adhesive strength of nc-TiN/a-Si_3N_4 as 46 GPa and compared it with tensile stress (33 GPa) at the periphery of contact between the coatings and the indenter following application of a maximum (70 mN) load. Herzian analysis applied to measuring tensile stress in glass was used in an earlier work by Argon et al. [169]. This procedure was employed to determine tensile (radial) stress for crack-free indentation in a variety of super- and ultrahard nanocomposites [92]. Radial tensile stress in such indentation represents the lower limit of tensile stress in nanocomposites and actually reaches an ideal value calculated for these materials. Detailed Herzian analysis of experimental indentation curves for nanocomposites and diamond confirmed the self-consistency of the results of these measurements and high hardness values obtained for the said materials [92, 107, 108, 122]. The results of numerical simulation by the finite element method (FEM) also confirm experimental data [92]. Other details can be found in the aforecited publications.

High 'crack toughness' in the materials under consideration is frequently applied because indentation at large loads (e.g., 1000 mN) does not cause defect formation in a 6–10-μm thick coating on a mild steel substrate with 20% stress (see paper [107] for confirmation of the reproducibility of these results). Thinner coatings show only circular (not radial)

Herzian cracks that should originate from the corners of the indentation region. These examples demonstrate the importance of very high resistance to brittle cracking in these materials. It does not mean, however, that they must just as well have high crack toughness described quantitatively by stress intensity factor K_1 or energy release rate. For a simple case of flat cracks of size $2a$, stress intensity factor $K_1 = \sigma(\pi a)^{0.5}$, where σ is the stress necessary for $2a$-sized crack propagation. The value of K_1 can be found by the indentation technique if radial cracks arise in the indentation corners and their length is much smaller than the sample thickness. This condition is difficult to meet for coatings. Nevertheless, the absence of radial cracks in many indentation experiments (such as reported by Veprek and some other researchers) in combination with high tensile stress is a characteristic feature of materials having a crack initiation threshold [92].

Apart from high brittle cracking resistance, nanocomposites show a high potential for recovery of elasticity (up to 94%) after imposing a load of 70 mN, when load-independent hardness exceeds 100 GPa [92] and the limit of elasticity after imposing a load of 1000 GPa is greater than 10%. For example, no cracks develop when a 6-μm thick coating is pressed by 1000 mN into a mild steel substrate ($H_V \approx 1.8$ GPa) to a depth of 2 μm. The hardness of a composite involving the coating and substrate remains equal to 40 GPa, and unloading results in a 10% recovery of the coating, despite the fact that it is practically held by excessively plastically deformed substrate [92]. The absence of cracks even beneath the coating surface was thoroughly verified by Herzian analysis and load curve evaluation [107].

As shown by Veprek et al. [19], all these properties are consistent with the defect-free nature of the material. Imagine glass of a perfect (defectless) structure. A stress-related change in internal energy roughly corresponds to a change in interatomic bonding energy integrated over the entire sample. Stress resistance, i.e., restoration (recovery) force acting to minimize the system's energy (interatomic distances and bond angles being brought to their equilibrium values) has been considered in Ref. [19]. Notice that the restoring force is the first derivative of internal energy in the presence of stress. The first derivative of tensile strength for equilibrium stress is the Young modulus, i.e., $E = (\mathrm{d}^2U/\mathrm{d}\varepsilon^2)_0$ (ε is the coefficient of elasticity). It should be mentioned that the elasticity modulus grows after compression ($\varepsilon < 0$) and decreases after stretching ($\varepsilon > 0$). Maximum tensile strength matches decohesion force σ_m achieved at maximum recovery stress (elastic limit) $\varepsilon_m \approx 15-20$ %, when interatomic covalent bonds break down under the effect of stress [19]. The entire interval $0 < \varepsilon < \varepsilon_m$ corresponds to elastic strain but is not linear due to the stress dependence of elastic moduli.

This line of reasoning leads to the conclusion that the extraordinary mechanical properties of superhard stable nanocomposites are easy to explain in terms of conventional fracture mechanics for materials that are free of cracks. Freshly prepared silicon fibers and whiskers (filamentous single crystals a few nanometers in thickness) have practically no cracks and stresses in them are close to ideal. As follows from Fig. 19 [19], stress in these materials is equivalent to that in stable nanocomposites.

Future studies should be designed to provide a deeper insight into the nature of nonlinear elastic response and the mechanism of plastic deformation in these materials. For example, bulk modulus B in the area under the indenter for coatings with hardness 50 – 60 GPa increases with a rise in pressure P as $B(P) \approx B(0) + 5P$, where $B(0)$ is the bulk modulus in the absence of pressure. A factor of proportionality of 5 measured by high-resolution X-ray diffraction method [170] agrees with the values predicted based on the UBER [124, 120]. For this reason, bulk modulus measured by the high-resolution X-ray diffraction method [170] for the coatings prepared by Veprek et al., $B(0) = 295 \pm 15$ GPa, increased with a rise in hardness up to 545 – 595 GPa (note that pressure under the indenter was roughly equal to $H = L/A_c$, where L is the indentation load, and A_c is the coating area). This makes the routine finite element method (FEM) unfit to resolve problems with strong nonlinearity even though a major part of elastic reaction after unloading occurs in regions lying far apart from the intender, where pressure grows insignificantly, while the stress value to be used in computation is rather high. Such a situation arises when the mechanism of plastic deformation operates in amorphous materials [122, 123]. FEM-assisted simulation of stresses yields very interesting data relevant to the problem under discussion [171, 197 – 199].

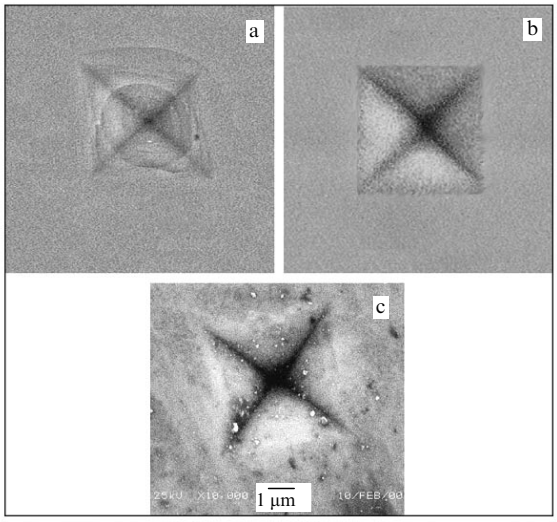

Figure 19. Scanning electron micrograms of indentation sites under a load of 1000 mN in a superhard coating: (a) 3.5-μm thick coating (load-invariant hardness $H_V \approx 105$ GPa, Fig. 12a); the coating is pressed deep into a mild steel substrate; (b) 10.7-μm thick coating (load-invariant hardness $H_V \approx 60$ GPa); (c) 6.1-μm thick ultrahard coating (load-invariant thickness $H_{0.005} \approx 100$ GPa, coating/substrate composite hardness is around 38 GPa). Note the absence of radial cracks in the diagonal direction in images (b) and (c) [19].

Figure 19 presents the results of hardness measurements obtained with the help of a nanoindenter for superhard (or ultrahard) coatings deposited onto different substrates (see also Fig. 12a, b). These data were reported by Veprek and coworkers in Refs [108] and [19] (see also Ref. [10]); they are discussed here to show how hardness was measured. Figure 19b, c displays no radial cracks in the diagonal direction in SEM images. According to the authors of Refs [19, 108, 139], the absence of radial cracks in many indentation experiments, coupled with the high tensile stress, is an intrinsic feature of materials having a crack initiation threshold [19].

Results in conflict with Veprek's and some other researchers' concept are borrowed from the relatively recent work [172]. It shows that high hardness and thermal stability are

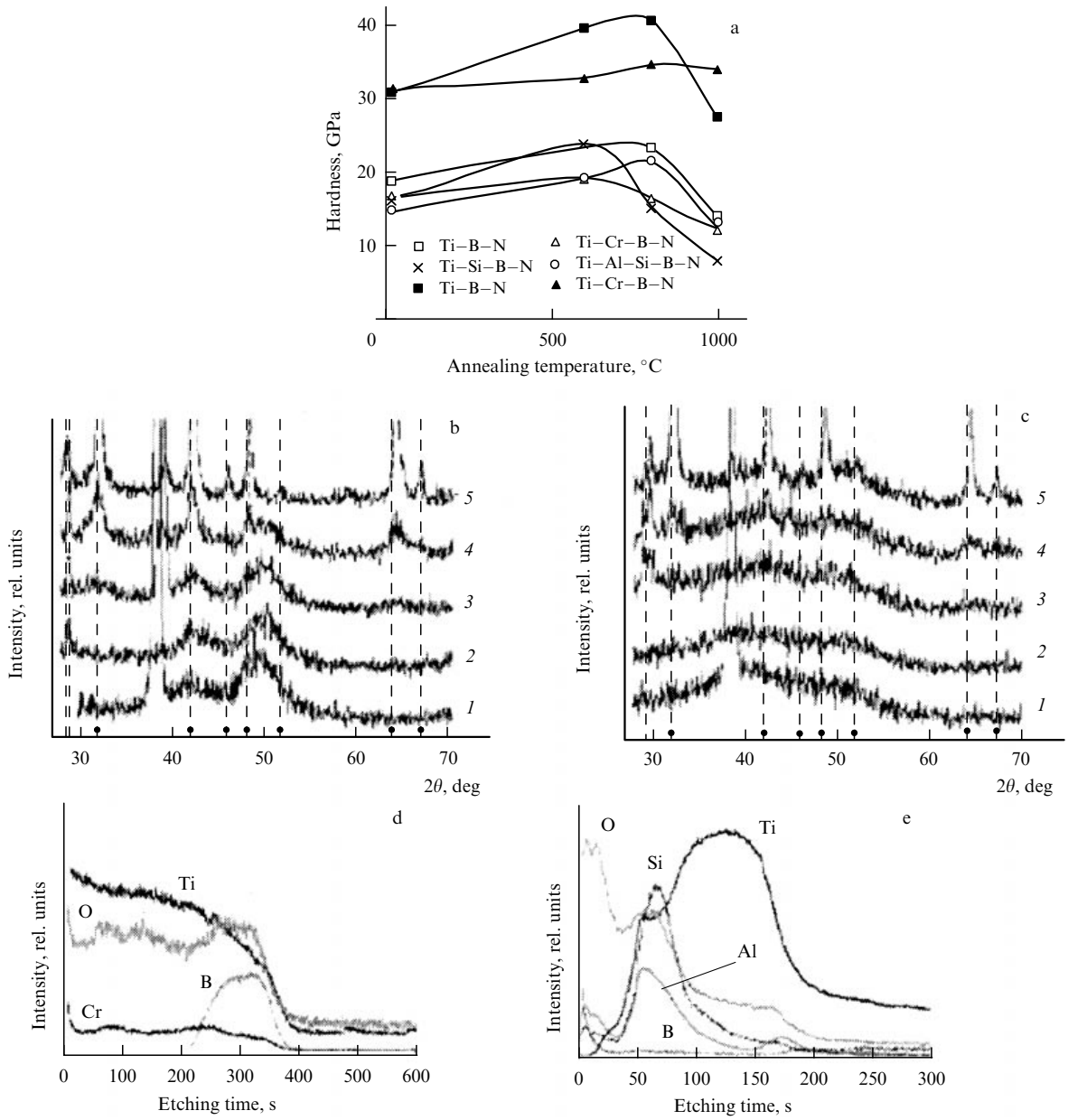

Figure 20. (a) Dependences of nanocomposite hardness on annealing temperature [172]. (b, c) X-ray diffraction spectra of Ti – Cr – B – N and Ti – Al – Si – B – N films before (*1*) and after annealing at 600 °C (*2*), 700 °C (*3*), 800 °C (*4*), and 900 °C (*5*) for 1 hour. (d) Thickness of the oxide layer in different films measured by SIMS. (e) SIMS depth profiles of a Ti – Al – Si – B – N film subjected to high-temperature oxidation at 800 °C [172].

very sensitive to the optimal coating structure (and not just to oxygen and carbon concentrations in the film). Figure 20a illustrates film hardness as a function of annealing temperature. It appears that hardness increased with annealing temperature from 15 – 20 to 20 – 25 GPa, reached a maximum at 600 – 800 °C, and sharply decreased to below initial values at 1000 °C. The hardness of Ti – B – N coatings grown under optimal conditions amounted to 30 GPa (Fig. 20a). It increased to 35 GPa (Ti – Cr – B – N coatings) and 41 GPa (Ti – B – N coatings) after annealing at 800 °C. The hardness of Ti – Cr – B – N deposited in optimal conditions remained unaltered up to 1000 °C. The authors of Ref. [172] evaluated oxidation resistance using the same films oxidized at 600, 700, 800, and 900 °C for 1 hour. Analysis by X-ray diffraction technique (Fig. 20b, c) and secondary ion mass spectrometry (SIMS) (Fig. 20d, e) revealed a single reflex in Ti – Cr – B – N films at $2\theta = 29°$, attributable to $TiBO_3$. The layer enriched in B formed and subsequently precluded oxygen penetration deep into the film. SIMS analysis demonstrated that only the surface layer contained Ti – O, while Ti – O – B lay beneath (Fig. 20d, e). A crystalline TiO_2 phase (rutile) could be seen only after annealing at 800 °C. Hence, the authors concluded that the formation of Al-, Si-, and B-rich oxide layers at the coating surface prevented its further oxidation. This barrier no longer hindered oxygen diffusion at temperatures above 900 °C. It was shown that B stabilizes the amorphous state due to the low mobility of atoms and prevents breakage of Si – N bonds at elevated temperatures by virtue of BN(C) formation. This finding was confirmed in other experiments by Vlček et al. [173]. Implantation of B into a film led to systematic reduction in the mass loss. These data provide additional evidence that the thin surface layer containing Ti,

B, and oxygen protects Ti – B – N films from further oxidation better than TiN.

The effect of the power of an inductively-coupled plasma (ICP) generator on the mechanical properties of tantalum nitride films was investigated by Lee et al. [203]. TaN films were grown on Si (100) substrate by the magnetron sputtering technique in the presence of ICP in mixed Ar/N_2 discharges at 20 Torr (2.67 Pa) and 350 °C. Structural analysis was performed by X-ray diffraction, Auger electron spectroscopy, and atomic force microscopy methods; hardness was measured by microindentation. The structure of TaN films changed with the power of the ICP generator (100 – 400 W) and nitrogen content f_{N_2} (0.1 – 0.15 Pa). An increase in the power in this range induced a hexagonal ε-TaN phase in the existing hexagonal γ-Ta_2N ($f_{N_2} = 0.1$ Pa) or cubic δ-TaN ($f_{N_2} = 0.125$ and 0.15 Pa) compounds; hardness also increased from 25 – 30 to about 70 GPa. Such significant hardness enhancement is supposed to be due to the contribution of dense fine-grain microstructure and its multiphase nature.

11. Adhesive strength and scratching damage of multicomponent nanocomposite coatings

In Refs [7, 10], the adhesion strength of Ti – (Ca,Zr) – (C,N,O,P)-based coatings was measured by scratching their surfaces with a Rockwell type diamond indenter under a progressively growing load (Fig. 21a). Shtansky et al. [10] conducted their tests and recorded physical characteristics at different loads and scratch lengths. The instant of adhesive and cohesive coating destruction was recorded either visually using an optical microscope with a digital camera or from a change in one of the following five parameters: acoustic emission, friction force, coefficient of friction, penetration depth, and residual scratch depth. Minimal (critical) load L_c resulting in coating destruction was assessed. To verify the significance of events related to destruction, the authors determined not only the moment of appearance of the first crack (L_e), but the partial coating peeling (L_{e2}) and plastic attrition of a coating (L_{e3}) as well; these parameters characterize coating adhesion to the substrate. Aggregate analysis of these parameters increases the reliability of the method and determination accuracy of critical load.

Figure 21b shows changes in four parameters, viz. acoustic emission (AE), coefficient of friction μ, indenter penetration depth h, and residual scratch depth h_f after unloading, following scratching under an increasing normal load P_n for a Ti – Zr – C – O – N system on a TiNi substrate. The first crack over 60 μm in length appeared at $L_e = 6.4$ N and $h = 7$ μm, as apparent from the optical microscopic image of the coating destruction zone.

It follows from Fig. 21c that the appearance of cracks is associated with peak acoustic emission. The relationship between the growing load (P_n) and coefficient of friction is described by an oscillating curve, i.e., a rise in friction coefficient is accompanied by a burst of acoustic emission and the slowing down of the penetration of the indenter into the coating.

TiNi is known to have a hardness of 4.8 GPa and an elasticity modulus ranging 59 – 66 GPa [10, 12]. Scratching material with a low E/H ratio should reveal contact elasticity; in that case plastic deformation behavior is less likely [10, 18]. In the course of translational movement, the indenter squeezes out some material, as apparent from the reduction

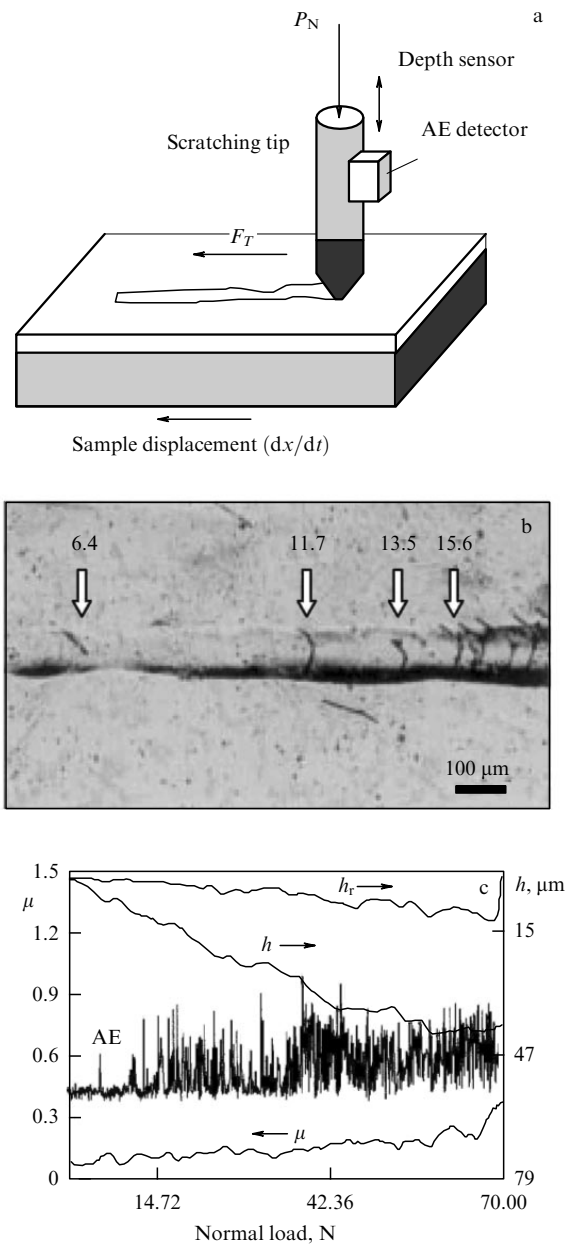

Figure 21. Schematic diagram and results of adhesion test: (a) results of the test for a Ti – Zr – C – O – N coating/TiNi substrate system; (b) coating structure in the zone of destruction under a loading of 5 – 18 N [10], and (c) dependences of AE, μ, h, h_r on the applied load.

in its penetration depth h (Fig. 21a) and the scratch width (Fig. 21b). The squeezing-out of the coating material may result in reversed plastic deformation (as evidenced by a small peak in the h_r versus load curve). As the indenter plows through the squeezed mass of the material, the coefficient of friction increases.

Both accumulation and relaxation of elastic strain energy are responsible for the formation of cracks; their initiation coincides with peak acoustic emission, while a local maximum in the $h(P_n)$ curve occurs when the coefficient of friction decreases to the initial value. As the process proceeds further, it becomes cyclic, i.e., each new crack (Fig. 21b) gives rise to an AE maximum (Fig. 21c). Hence, the substrate material appears at the scratch bottom only after the load increases to $L_{e3} \gtrsim 50$ N, which testifies to the high adhesion strength of the

coating. The indenter penetration depth at 50 N being $h = 38.8$ μm and residual depth $h = 6.2$ μm, elastic recovery after unloading was estimated at 82.7%.

12. Prospects for the field

Further research in the field of nanostructured films will be carried out along the following lines: (1) the formation of films with controllable grain size in the range from 1 to 10 nm for the elucidation of the relationship between their properties and dimensional parameters, and the production of new improved coatings with unique physical and functional characteristics; (2) nanocrystalization from the amorphous phase; (3) the transfer of electron charges between nanograins of different chemical compositions and Fermi energy; (4) the preparation of new protective coatings with an oxidation resistance higher than 2000 °C, and (5) the development of new systems for deposition of nanostructured coatings by physical methods. It may be expected that thin nanostructured films will be used in the near future as experimental models for manufacturing nanostructured bulk materials with tailored properties.

To date, TiN, TiNCr, and TiZrN coatings and TiN/CrN, MoN/TiAlN multilayer coatings, and some other materials have found a variety of applications in industry. Implantation of certain additional components (e.g., Si or B) into TiN films can significantly improve their physical and mechanical properties and thereby widen the spectrum of their application. The use of thin coatings was fairly well described in the recently published review [7] dealing with applications of multifunctional nanostructured films. Table 3 presents a few examples of the application of tribological superhard nanostructured coatings composed of immiscible phases (see also references [33, 37–45, 47] in this review). It is shown that doping classical TiN coatings with Si, B, Al, or Cr ensures a combination of high hardness and durability with a sufficiently low coefficient of friction [174, 175]. These multicomponent nanostructured coatings and films may be used to protect surfaces of different articles and instruments [182–191], such as cutting and stamping tools, casting rollers, parts of aircraft engines, gas-driven turbines and compressors, sliding bearings, and extrusion nozzles for glass and mineral fibers, against the simultaneous actions of high temperatures, mechanical wear, and aggressive media [7]. Other promising fields of application of these coatings include magnetic optics, electronic engineering, and medicine (DNA synthesis) [200–205]. Moreover, coatings are needed to develop a new generation of biocompatible materials, e.g., orthopedic and dental implants, materials for cranial and maxillofacial surgery, and the fixation of the cervical and lumbar spine, as described at greater length in review articles [7, 201].

13. Conclusions

This review concerns one of the mainstream areas of materials science, namely, the creation of new hard and superhard nanocomposite and nanostructured coatings. The possibilities of manipulating their properties and principal fields of application are considered. The large area (volume fraction up to 50%) and strength of the interfaces in these coatings greatly promote an increase in their strain resistance. The absence of dislocations inside crystallites contributes to the

Table 3. Examples of tribological superhard nanostructured films comprising immiscible phases (see review [7] and references cited therein).

Coating	Target composition	Film phase composition	Literature (references taken from review [7])
Ti–B–C–N	TiB + Ti or TiB_2 + TiC	nc-TiC + nc-TiB_2 + a-BN	[37]
Ti–B–N	TiB_2 + TiN or TiB_2 + Ti	nc-TiN + nc-TiB_2 (or a-TiB_2) + a-BN	[33, 36, 38]
Ti–Si–N	Ti_5Si_3 + Ti	nc-TiN + nc-$TiSi_2$ + a-Si_3N_4	[39]
	a*	nc-TiN + a-Si_3N_4	[40]
Ti–Cr–B–N	TiB + Ti_9Cr_4B + Cr_2Ti	nc-TiN + CrB_2 + a-BN + a-TiB_2	[33]
Ti–C–B	TiC + TiB_2	nc-TiB_2 + TiC + a-B_4C	
Ti–Si–B–N	TiB_2 + Ti_5Si_3 + Si or TiB_2 + Si	nc-TiB_2 + TiN + nc-$TiSi_2$ + a-Si_3N_4	[35, 36]
Ti–Si–C–N	TiC + Ti_5Si_3 or TiC + Ti_5SiC_2 + $TiSi_2$ + SiC	nc-TiC + nc-Ti_2SiC_2 + nc-$TiSi_2$ + SiC + a-Si_3N_4	[36, 42]
Ti–Al–B–N	TiAlBN	nc-TiB_2 + nc-$(Ti_xAl_{1-x})N$ + a-BN + a-AlN	[1]
Ti–Al–C–N	TiAl + TiC	nc-TiC + nc-$(Ti_xAl_{1-x})N$ + a-AlN	[36]
W–C	W + laser ablation of C	nc-WC + a-C	[43]
W–Si–N	b*	nc-W_2N + a-Si_3N_4	[44]
Ti–C	$TiC_{0.5}$	nc-TiC + a-C	[45]
Ti–Al–Si–N	TiN + TiAl	nc-$(Ti_xAl_{1-x})N$ + a-Si_3N_4	[46]
Cr–Si–N	Cr + Si	nc-CrN + a-Si_3N_4	[47]
Cr–B–N	CrB_2	nc-CrB_2 + a-BN	[33]

Notes: Most films were prepared by magnetron sputtering of targets in an atmosphere of Ar or N_2/Ar; a*: films obtained by chemical vapor deposition (CVD); b*: films obtained by thermal annealing of amorphous W–Si–N layers.

elasticity of these materials, permits purposefully changing their mechanical properties and reaching high values of hardness ($H \lesssim 40$ GPa), elastic recovery ($W_e \lesssim 70\%$), strength, and heat and corrosion resistances. Moreover, the coatings may differ in elasticity modulus, resistance to elastic breaking strain, and plastic resistance (H^3/E^2).

The authors are fully aware that the review cannot pretend to provide a comprehensive analysis of all original works concerning the problem under consideration (to our knowledge, over 900 papers have been published or accepted for publication in journals, volumes of collected articles, proceedings of domestic and international conferences, etc. over the last 3.5 years). Yet we tried to do our best to refer to and cover all major studies of leading specialists in the field, to analyze them, and to consider current concepts of physical processes proceeding in the structure of hard nanocomposite coatings and during their preparation. It should be noted by way of criticism that we put in question the validity of some cited values of hardness comparable with or exceeding natural diamond hardness or cubic boron nitride hardness as resulting from possible methodical errors. The errors might be related not only to the wrong choice of film thickness and indentation load but also to the use of diamond pyramids with finite hardness from 100 to 120 GPa. Thus, new methods for the assessment of hardness are needed, including non-destructive ones, especially for superhard coatings and ultrahard materials.

Special experiments should be designed to obtain a better understanding of the physical processes of self-strengthening and incomplete spinodal phase segregation. A slow positron beam [177 – 179] or a scanning positron microscope [192, 193] must be used to analyze the evolution (diffusion) of vacancy defects, viz. mono- and di-vacancies, vacancy clusters, 'vacancy + impurity atom' complexes and some others. Both simultaneous and successive application of a proton or helium ion microbeam and the use of proton-induced X-ray emission (PIXE), Rutherford back scattering (RBS) [179 – 181], and possibly nuclear reaction analysis (NRA) will help to trace atomic motion along nanograin boundaries and phase segregation processes in such structures as nc-TiN/a-Si_3N_4, Ta – Si – N, and Ti – B – N. A very thin interlayer (as thick as one or two monolayers), if created, will make possible the use of nanobeam electron spectroscopy (see relevant reference in paper [194]). Moreover, special attention must be given to elucidating the lower oxygen concentration limit and its influence on the thermal stability and hardness of nanocomposites or nanostructured coatings with the possible use of oxygen elastic resonance (or NRA), ion microbeams, or electron nanobeams [194]. The sensitivity of this method amounts to 10^{-1} (in fractions of a monolayer) and 10 – 10,000 Å (effective depth of analysis) without etching of a sample surface. Examples of studies using these methods can be found in Refs [177 – 181]; the authors combined slow positron beam and microbeam of protons and helium ions with PIXE and RBS for the analysis of segregation at grain boundaries in iron implanted with Al, C, and Ti ions and of vacancy defect evolution (diffusion), e.g., in the case of annealing with a high-current electron beam [180].

The authors are pleased to express gratitude to their colleagues who kindly donated reprints of their papers. Thanks are due to R A Andrievskii, I I Aksenov, A Cavaleiro, A D Korotaev, E A Levashov, J Musil, D V Shtansky, V E Strel'nitskii, S Vepřek, and many others for their critical remarks and helpful discussions concerning separate sections of this review. We are grateful to S N Bratushka, Yu A Kravchenko, and A N Shipilenko of the Institute of Surface Modification, Sumy, and to M A Vasil'ev and V N Uvarov (G V Kurdyumov Institute for Metal Physics, National Academy of Sciences of Ukraine) for assistance and encouragement in considering the topic of the review.

The work was supported in part by the National Academy of Sciences of Ukraine (Project Nanotechnologies, Nanofilms and Nanomaterials: New principles for the creation of nanocomposite materials, coatings, and films with the help of ion, plasma, and electron beams) and by ISTC (Project K-1198).

References

1. Gleiter H *Acta Mater.* **48** 1 (2000)
2. Skorokhod V V, Ragulya A V, in *Progresivni Materiali i Tekhnologii* (Progressive Materials and Technologies) Vol. 2 (Kyiv: Akademperiodika, 2003) p. 7
3. Andrievskii R A, Glezer A M *Fiz. Met. Metalloved.* **88** (1) 50 (1999) [*Phys. Met. Metallogr.* **88** 45 (1999)]
4. Cavaleiro A, De Hosson J Th M (Eds) *Nanostructured Coatings* (New York: Springer, 2006)
5. Mayrhofer P H et al. *Prog. Mater. Sci.* **51** 1032 (2006)
6. Andrievski R A *Usp. Khim.* **74** 1163 (2005) [*Russ. Chem. Rev.* **74** 1061 (2005)]
7. Levashov E A, Shtansky D V *Usp. Khim.* **76** 501 (2007) [*Russ. Chem. Rev.* **76** 463 (2007)]
8. Voevodin A A et al. (Eds) *Nanostructured Thin Films and Nanodispersion Strengthened Coatings* (Dordrecht: Kluwer Acad. Publ., 2004)
9. Reshetnyak E N, Strel'nitskii V E "Sintez nanostrukturnykh plenok: dostizheniya i perspectivy" ("Synthesis of nanostructured films: achievements and prospects"), in *Khar'kovskaya Nanotekhnologicheskaya Assambleya. Sbornik Dokladov* (Collected Reports of Khar'kov's Nanotechnology Assembly) (Eds I M Neklyudov, A P Shpak, V M Shulaev) Vol. 1 (Khar'kov, 2007) p. 6
10. Shtansky D V et al. *Fiz. Tver. Tela* **47** 242 (2005) [*Phys. Solid State* **47** 252 (2005)]
11. Kiryukhantsev-Korneev F V et al. *Fiz. Met. Metalloved.* **97** (3) 96 (2004) [*Phys. Met. Metallogr.* **97** 314 (2004)]
12. Shtansky D V et al. *J. Mater. Synth. Process* **6** 61 (1998)
13. Beresnev V M et al. *Fiz. Inzh. Poverkh.* **5** (1/2) 4 (2007)
14. Beresnev V M et al. *Visn. Khar'kivs'k. Univ. Ser. Yadra, Chastinki, Polya* (2(34)) 93 (2007)
15. Pogrebnyak A D, Tyurin Yu N *Usp. Fiz. Nauk* **175** 515 (2005) [*Phys. Usp.* **48** 487 (2005)]
16. Boiko V I, Valyaev A N, Pogrebnyak A D *Usp. Fiz. Nauk* **169** 1243 (1999) [*Phys. Usp.* **42** 1139 (1999)]
17. Kadyrzhanov K K et al. *Ionno-Luchevaya i Ionno-Plazmennaya Modifikatsiya Materialov* (Materials Modification by Ion Beams and Ion Plasma) (Moscow: Izd. MGU, 2005)
18. Azarenkov N A, Beresnev V M, Pogrebnjak A D *Struktura i Svoistva Zashchitnykh Pokrytii i Modifitsirovannykh Sloev Materialov* (Structure and Properties of Protective Coatings and Modified Layers of Materials) (Khar'kov: Khar'kov Nation. Univ. Publ., 2007)
19. Veprek S et al. *Thin Solid Films* **476** 1 (2005)
20. Gleiter H *Prog. Mater. Sci.* **33** 223 (1989)
21. Yip S *Nature* **391** 532 (1998)
22. Musil J, Vlček J *Mater. Chem. Phys.* **54** 116 (1998)
23. Vepřek S *J. Vac. Sci. Technol. A* **17** 2401 (1999)
24. Musil J *Surf. Coat. Technol.* **125** 322 (2000)
25. Voevodin A A, Zabinski J S *Thin Solid Films* **370** 223 (2000)
26. Brazhkin V V et al. *Philos. Mag. A* **82** (2) 231 (2002)
27. Musil J et al. *Key Eng. Mater.* **230 – 232** 613 (2002)
28. Musil J *Acta Metallurg. Sinica* **18** (3) 433 (2005)
29. Zhang S et al. *Surf. Coat. Technol.* **198** 2 (2005)
30. Musil J, in *Nanostructured Hard Coatings* (New York: Kluwer Acad./Plenum Publ., 2005) Ch. 10
31. Tsui T Y et al. *Mater. Res. Soc. Symp. Proc.* **383** 447 (1995)

32. Musil J et al. *Surf. Coat. Technol.* **154** 304 (2002)
33. Musil J, Jirout M, in *5th Asian-European Intern. Conf. on Plasma Surface Engineering, Sept. 12–16, 2005 Qingdao City, China*; *Surf. Coat. Technol.* **201** 5148 (2007)
34. Zeman H, Musil J, Zeman P *J. Vacuum Sci. Technol. A* **22** 646 (2004)
35. Musil J et al. *Thin Solid Films* **478** 238 (2005)
36. Musil J, Dohnal P, Zeman P *J. Vacuum Sci. Technol. B* **23** 1568 (2005)
37. Musil J, Zeman P *Solid State Phenomena* **127** 31 (2007)
38. Musil J "Properties of hard nanocomposite thin films", in *Nanocomposite Thin Films and Coatings*: *Processing, Properties and Performance* (Eds S Zhang, A Nasar) (London: Imperial College Press, 2007) Ch. 5
39. Linder C et al. *Sens. Actuators A* **61** 387 (1997)
40. Lee Y-J et al. *Thin Solid Films* **320** 141 (1998)
41. Nah J W, Hwang S K, Lee C M *Mater. Chem. Phys.* **62** 115 (2000)
42. Nah J W et al. *Surf. Coat. Technol.* **123** 1 (2000)
43. Olowolafe J O et al. *Thin Solid Films* **365** 19 (2000)
44. Münz W-D *J. Vac. Sci. Technol. A* **4** 2717 (1986)
45. Donohue L A et al. *Surf. Coat. Technol.* **94–95** 226 (1997)
46. Wadsworth I et al. *Surf. Coat. Technol.* **94–95** 315 (1997)
47. Veprek S, Haussmann M, Reiprich S *Mater. Res. Soc. Symp. Proc.* **400** 261 (1996)
48. Holleck H *J. Vac. Sci. Technol. A* **4** 2661 (1986)
49. Berg C et al., in *Handbook of Ceramic Hard Materials* (Ed. R Riedel) (Weinheim: Wiley-VCH, 2000) Table I, p. 968
50. Korotaev A D et al. *Fiz. Khim. Obrabotki Mater.* (1) 22 (2004)
51. Korotaev A D, Tyumentsev A N, Litovchenko I Yu *Phys. Met. Metallogr.* **90** (Suppl. 1) 36 (2000)
52. Tyumentsev A N et al., in *Proc. of the 1st Intern. Congress on Radiation Physics, High-Current Electronics, and Materials Modification* Vol. 3 (Tomsk, 2000) p. 442
53. Morris D G, in *Materials Science Foundation* Vol. 2 (Translation technical publication LVD Switzerland, Germany, UK, USA) (1998) p. 1
54. Musil J *Physical and Mechanical Properties of Hard Nanocomposite Films Prepared by Reactive Magnetron Sputtering* (Eds A Cavaleiro, J Tm M De Hosson) (New York: Springer, 2006) Ch. 10
55. Zeman P et al. *Mater. Sci. Eng. A* **289** 189 (2000)
56. Vlček J et al. *Surf. Coat. Technol.* **76–77** 274 (1995)
57. Musil J, Matous J, Valvoda V *Vacuum* **46** 203 (1995)
58. Musil J, Vlček J "Physical and mechanical properties of hard nanocomposite films prepared by magnetron sputtering", in *Proc. of the 1st Intern. Congress on Radiation Physics, High-Current Electronics, and Materials Modification* Vol. 3 (Tomsk, 2000) p. 393
59. Vepřek S et al. *Surf. Coat. Technol.* **108–109** 138 (1998)
60. Vepřek S et al. *J. Vac. Sci. Technol. A* **21** 532 (2003)
61. Zhang R F, Vepřek S *Mater. Sci. Eng. A* **448** 111 (2007)
62. Riedel R (Ed.) *Handbook of Ceramic Hard Materials* (Weinheim: Wiley-VCH, 2000)
63. Rogl P, Schuster J C *Phase Diagrams of Ternary Boron Nitride and Silicon Nitride Systems* (Materials Park, OH: ASM Intern., 1992)
64. Blanquet E et al., in *Chemical Vapor Deposition*: *Proc. of the 14th Intern. Conf. and EUROCVD-11, Paris, September 5–9, 1997* (Electrochem. Soc. Proc., Vol. 97-25, Eds M D Allendorf, C Bernard) (Pennington, NJ: The Electrochem. Soc., 1997) p. 23
65. Hirai T, Hayashi S *J. Mater. Sci.* **17** 1320 (1982); Hayashi S et al. *J. Mater. Sci.* **17** 3336 (1982); Hirai T, Hayashi S *J. Mater. Sci.* **18** 2401 (1983)
66. Mayrhofer P H et al. *Appl. Phys. Lett.* **86** 131909 (2005)
67. Mayrhofer P H, in *Nanostructured Thin Films and Nanodispersion Strengthened Coatings* (Eds A A Voevodin et al.) (Dordrecht: Kluwer Acad. Publ., 2004) p. 57
68. Vepřek S, Reiprich S *Thin Solid Films* **268** 64 (1995)
69. Vepřek S, Haussmann M, Reiprich S *J. Vac. Sci. Technol. A* **14** 46 (1996)
70. Knotek O, in *Mater. Res. Soc., Fall Meeting/ICEM, Boston, MA, USA, Dec. 2–6, 1996* (unpublished and private communication)
71. Knotek O et al. *Mater. Sci. Eng. A* **209** 394 (1996)
72. Voevodin A A, Zabinski J S *Thin Solid Films* **370** 223 (2000)
73. Hauert R, Patscheider J *Adv. Eng. Mater.* **2** 247 (2000)
74. Li D et al. *Appl. Phys. Lett.* **67** 203 (1995)
75. Li D et al. *Appl. Phys. Lett.* **68** 1211 (1996)
76. Chung Y W *Surf. Rev. Lett.* **3** 1597 (1996)
77. Zhang R F, Sheng S H, Veprek S *Appl. Phys. Lett.* **91** 031806 (2008)
78. Li S Z, Shi Y, Peng H *Plasma Chem. Plasma Process.* **12** 287 (1992)
79. Vepřek S, Reiprich S, Li S *Appl. Phys. Lett.* **66** 2640 (1995)
80. Niederhofer A et al. *Surf. Coat. Technol.* **146–147** 183 (2001)
81. Veprek A et al. *Mater. Res. Soc. Symp. Proc.* **581** 321 (2000)
82. Veprek S et al. *Surf. Coat. Technol.* **133–134** 152 (2000)
83. Li S Z et al., unpublished
84. Lawn B *Fracture of Brittle Solids* 2nd ed. (Cambridge: Cambridge Univ. Press, 1993) p. 173
85. Andrievski R A *J. Solid State Chem.* **133** 249 (1997)
86. Hammer P et al. *Surf. Coat. Technol.* **68–69** 194 (1994)
87. Mitterer C et al. *Surf. Coat. Technol.* **120–121** 405 (1999)
88. Männling D-H et al. *Surf. Coat. Technol.* **146–147** 263 (2001)
89. Karvánková P et al. *Surf. Coat. Technol.* **146–147** 280 (2001)
90. Karvankova P et al. *Surf. Coat. Technol.* **163–164** 149 (2003)
91. Hultman L *Vacuum* **57** 1 (2000)
92. Musil J, Baroch P, Zeman P, in *Plasma Surface Engineering Research and Its Practical Applications* (Ed. R Wei) (Kerala: Signpost Publ., 2007) Ch. 1
93. Zeman P, Musil J *Appl. Surf. Sci.* **252** 8319 (2006)
94. Vepřek S et al. *Surf. Coat. Technol.* **86–87** 394 (1996)
95. Hertzberg R W *Deformation and Fracture Mechanics of Engineering Materials* 3rd ed. (New York: Wiley, 1989)
96. Veprek S, Veprek-Heijman M G J, in *Nanostructured Coatings* (Eds A Cavaleiro, J Th M De Hosson) (New York: Springer, 2006)
97. Vaz F, PhD Thesis (Portugal: Univ. of Minho, 2000)
98. Veprek S et al. *Mater. Sci. Eng. A* **448** 366 (2007)
99. Procházka J et al. *Mater. Sci. Eng.* **384** 102 (2004)
100. Holubar P, Jilek M, Sima M *Surf. Coat. Technol.* **133–134** 145 (2000)
101. Männling D-H, Diploma Work (Münich: Technical Univ. of Münich, 1999)
102. Patscheider J *MRS Bull.* **28** (3) 180 (2003)
103. Meng W J et al. *J. Mater. Res.* **17** 2628 (2002)
104. Zhang X D et al. *Surf. Coat. Technol.* **177–178** 325 (2004)
105. Lee E-A, Kim K H *Thin Solid Films* **420–421** 371 (2002)
106. Vaz F et al. *Surf. Coat. Technol.* **133–134** 307 (2000)
107. Veprek S et al. *Surf. Coat. Technol.* **200** 3876 (2006)
108. Veprek S et al. *Thin Solid Films* **436** 220 (2003)
109. Doener M F, Nix W D *J. Mater. Res.* **1** 601 (1986)
110. Pharr G M *Mater. Sci. Eng. A* **253** 151 (1998)
111. Bull S J, Page T F, Yoffe E H *Philos. Mag. Lett.* **59** 281 (1989)
112. Fischer-Cripps A C *Nanoindentation* (New York: Springer, 2002)
113. Bull S J *J. Vac. Sci. Technol. A* **19** 1404 (2001)
114. Bull S J *Thin Solid Films* **398–399** 291 (2001)
115. Hu X et al. *J. Vac. Sci. Technol. A* **20** 1921 (2002)
116. Vaz F et al. *Surf. Coat. Technol.* **146–147** 274 (2001)
117. Winters H F, Sigmund P *J. Appl. Phys.* **45** 4760 (1974)
118. Winters H F, in *Plasma Chemistry* Vol. III (Eds S Vepřek, M Venugopalan) (Berlin: Springer-Verlag, 1980) p. 69
119. Musil J et al. *Mater. Sci. Eng. A* **340** 281 (2003)
120. Veprek S et al. *Mater. Sci. Eng. A* **340** 292 (2003)
121. Tabor D *The Hardness of Metals* (Oxford: Clarendon Press, 1951)
122. Argon A S, Veprek S *Mater. Res. Soc. Symp. Proc.* **697** 3 (2002)
123. Argon A S, Demkowicz M J, Veprek S *AIP Conf. Proc.* **712** 3 (2004)
124. Rose J H et al. *Phys. Rev. B* **29** 2963 (1984)
125. Smith J R et al., in *Chemistry and Physics of Fracture* (Eds R M Latanision, R H Jones) (Dordrecht: Kluwer Acad. Publ., 1987)
126. Murarka S P *J. Vac. Sci. Technol.* **17** 775 (1980)
127. Suzuki T et al. *J. Mater. Sci.* **35** 4193 (2000)
128. Bull S J, Hainsworth S V *Surf. Coat. Technol.* **122** 225 (1999)
129. Héau C, Terrat J P *Surf. Coat. Technol.* **108–109** 332 (1998)
130. Schmalzried H *Chemical Kinetics of Solids* (Weinheim: VCH, 1995)
131. Porter D A, Easterling K E *Phase Transformations in Metals and Alloys* 2nd ed. (Cheltenham: Stanley Thornes Publ., 2001)
132. Vepřek S et al. *Surf. Coat. Technol.* **108–109** 138 (1998)
133. Procházka Th J "Superharte TiN/Si_3N_4 Nanokomposite durch reaktive Magnetronzerstübung kombiniert mit chemischer Gasphaseabscheidung", PhD Thesis (Münich: Technical Univ. of Münich, 2003); http://tumb1.biblio.tu-muenchen.de/publ/diss/ch/2003/ prochazka.pdf

134. Karvánková P "Superhard nc-TiN/a-BN/a-TiB_2 and nc-MnN/a-metal nanocrystalline composite coatings", PhD Thesis (Münich: Technical Univ. of Münich, 2003); http://tumb1.biblio.tu-muenchen.de/publ/diss/ch/2003/karvankova.pdf
135. Maennling D-H, PhD Thesis (Münich: Technical Univ. of Münich, 2003); http://tumb1.biblio.tu-muenchen.de/publ/diss/ch/2003/maennling.pdf
136. Karvánková P et al. *Surf. Coat. Technol.* (in press)
137. Karvánková P et al. *Thin Solid Films* **467** 133 (2004)
138. Chase M W et al. "JANAF Thermochemical Tables" *J. Phys. Chem. Ref. Data* **14** (Suppl. 1) (1985) 3rd ed.
139. Veprek S et al. *Mater. Sci. Eng. A* **366** 202 (2004)
140. Gahn J W *Acta Metall.* **11** 1275 (1963)
141. Diserens M, Patscheider J, Lévy F *Surf. Coat. Technol.* **120 – 121** 158 (1999)
142. Diserens M, Patscheider J, Lévy F *Surf. Coat. Technol.* **108 – 109** 241 (1998)
143. Patscheider J, Zehnder T, Diserens M *Surf. Coat. Technol.* **146 – 147** 201 (2001)
144. Hauert R et al. *Adv. Mater.* **11** 175 (1999)
145. Mayrhofer P H et al. *Appl. Phys. Lett.* **83** 2049 (2003)
146. Münz W-D *J. Vac. Sci. Technol. A* **4** 2717 (1986); Veprek S et al. *Thin Solid Films* **476** 1 (2005), see p. 28
147. Münz W-D *Werkst. Korros.* **41** 753 (1990)
148. Münz W-D et al., in *Proc. of Industrial Tooling 2001, September 5 – 6, Southampton* (Southampton: Centaur Publ., 2001) p. 1
149. Tanaka Y et al. *Surf. Coat. Technol.* **146 – 147** 215 (2001)
150. Bunshah R F (Ed.) *Handbook of Deposition Technologies for Films and Coatings* 2nd ed. (Park Ridge, NJ: Noyes Publ., 1994)
151. Beresnev V M et al. *Phys. Surf. Eng.* **5** (1/2) 4 (2007)
152. Li Z et al. *Jpn. J. Appl. Phys.* **42** 7510 (2003)
153. Watanabe H et al. *Surf. Coat. Technol.* **169 – 170** 452 (2003)
154. Nose M et al. *Surf. Coat. Technol.* **174 – 175** 261 (2003)
155. Zhang C H et al. *J. Appl. Phys.* **95** 1460 (2004)
156. Nose M et al. *J. Vac. Sci. Technol. A* **20** 823 (2002)
157. Gleiter H *Nanostruct. Mater.* **6** 3 (1995)
158. Siegel R W, Fougere G E *Nanostruct. Mater.* **6** 205 (1995)
159. Malik A, Rawat R J (Eds) *New Nanotechniques* (New York: Nova Science Publ., 2009)
160. Carsley J E et al. *Nanostruct. Mater.* **5** 441 (1995)
161. Weertman J R et al. *MRS Bull.* **24** (2) 44 (1999)
162. Gleiter H *Nanostruct. Mater.* **6** 3 (1996)
163. Argon A S, in *Physical Metallurgy* Vol. 3, 4th ed. (Eds R W Cahn, P Haasen) (Amsterdam: North-Holland, 1996) p. 1878
164. Argon A S, in *Materials Science and Technology: A Comprehensive Treatment* (Eds R W Cahn, P Haasen, E J Kramer) (Weinheim: VCH, 1993) p. 461
165. Demkowicz M J, Argon A S *Phys. Rev. Lett.* **93** 025505 (2004)
166. Gouldstone A, Van Vliet K J, Suresh S *Nature* **411** 656 (2001)
167. Van Vliet K J et al. *Phys. Rev. B* **67** 104105 (2003)
168. Jacobs K et al. *Science* **293** 1803 (2001)
169. Argon A S, Hori Y, Orowan E *J. Am. Ceram. Soc.* **43** 86 (1960)
170. Veprek S et al. *Mater. Res. Soc. Symp. Proc.* **750** 9 (2003)
171. Karvánková P et al. *Surf. Coat. Technol.* **200** 2978 (2006)
172. Kiryukhantsev-Korneev Ph V et al. *Surf. Coat. Technol.* **201** 6143 (2007)
173. Vlček J et al. *J. Vac. Sci. Technol. A* **23** 1513 (2005)
174. Shtansky D V et al. *J. Mater. Synth. Procces.* **6** 61 (1998)
175. Mayrhofer P M, Clemens H, Mitterer S *Z. Metall.* **96** 5 (2005)
176. Jiang N et al. *Mater. Sci. Eng. B* **106** 163 (2004)
177. Lavrent'ev V I, Pogrebnyak A D, Shandrik R *Pis'ma Zh. Eksp. Teor. Fiz.* **65** 86 (1997) [*JETP Lett.* **65** 91 (1997)]
178. Pogrebnyak A D et al. *Pis'ma Zh. Eksp. Teor. Fiz.* **27** (14) 88 (2001) [*JETP Lett.* **27** 615 (2001)]
179. Lavrent'yev V I, Pogrebnyak A D, Shandrik R *Pis'ma Zh. Eksp. Teor. Fiz.* **65** 618 (1997) [*JETP Lett.* **65** 651 (1997)]
180. Pogrebnjak A D et al. *Phys. Lett. A* **241** 357 (1998)
181. Pogrebnjak A D, Tolopa A M *Nucl. Instrum. Meth. Phys. Res. B* **52** 25 (1990)
182. Vasil'ev M A, Prokopenko G I, Filatova V S *Usp. Fiz. Met.* (5) 345 (2004)
183. Shevchenko S V, Stetsenko N N *Usp. Fiz. Met.* (4) 219 (2004)
184. Larikov L N *Metallofiz. Noveishie Tekhnol.* **17** (9) 56 (1994)
185. Pozdnyakov V A *Fiz. Met. Metalloved.* **96** (1) 114 (2003) [*Phys. Met. Metallogr.* **96** 105 (2003)]
186. Larikov L N *Metallofiz. Noveishie Tekhnol.* **19** (1) 19 (1993)
187. Gautier C, Machet J *Thin Solid Films* **295** 43 (1997)
188. Strel'nitskii V E, Aksenov I I *Pleonki Almazopodobnogo Ugleroda* (Films of Diamond-Like Carbon) (Khar'kov: NNTs KhFTI, 2006)
189. Firstov S A et al., in *Progresivni Materiali i Tekhnologii* Vol. 2 (Kyiv: Akademperiodika, 2003) p. 610
190. Goncharenko I M et al. "Formirovanie nanokristallicheskikh Ti – Cu – N-pokrytii v plazme dugovykh razryadov nizkogo davleniya" ("Formation of nanocrystalline Ti – Cu – N coatings in low-pressure arc discharge plasma"), in *Doklady 7 Mezhdunarod. Konf. "Vakuumnye Nanotekhnologii i Oborudovanie"* (Khar'kov: NNTs KhFTI, IPP "Kontrast", 2006) p. 221
191. Kunchenko V V et al. *Vopr. Atom. Nauki Tekh. Ser. Fiz. Radiatsion. Povrezhdenii Radiatsion. Materialoved.* (4) 185 (2006)
192. David A et al. *Mater. Sci. Forum* **255 – 257** 205 (1997)
193. Krause-Rehberg R, Leipner H S *Positron Annihilation in Semiconductors: Defects Studies* (Berlin: Springer-Verlag, 1999)
194. Renk T J et al. *Proc. IEEE* **92** 1057 (2004)
195. Zeman P, Musil J, Daniel R *Surf. Coat. Technol.* **200** 4091 (2006)
196. Musil J et al. *Surf. Coat. Technol.* **200** 3886 (2006)
197. Zhang R F, Sheng S H, Veprek S *Appl. Phys. Lett.* **91** 031906 (2007)
198. Zhang R F, Veprek S *Phys. Rev. B* **76** 174105 (2007)
199. Veprek S, Argon S, Zhang R F *Philos. Mag. Lett.* **87** (12) 955 (2007)
200. Mirkin Ch A *MRS Bull.* **25** (1) 43 (2000)
201. Muster D et al. *MRS Bull.* **25** (1) 25 (2000)
202. Murray C B et al. *MRS Bull.* **26** (12) 985 (2001)
203. Lee G R et al. *Surf. Coat. Technol.* **201** 5207 (2007)
204. Ragulya A V, Skorokhod V V *Konsolidirovannye Nanostrukturnye Materialy* (Consolidated Nanostructured Materials) (Kyiv: Naukova Dumka, 2007)
205. Beresnev V M et al. *Usp. Fiz. Met.* **8** (3) 171 (2007)